FRACTURE MECHANISMS OF ALSI10MG PRODUCED THROUGH SLM

THE EFFECT OF POST PROCESSING ON THE MECHANICAL PROPERTIES AND FRACTURE MECHANISMS OF ALSI10MG PRODUCED THROUGH SELECTIVE LASER MELTING

By YOUSSEF SALIB, B. ENG

A Thesis Submitted to the School of Graduate Studies in Partial Fulfilment of the Requirements for the Degree Master of Applied Science

McMaster University MASTER OF APPLIED SCIENCE (2023) Hamilton, Ontario (Materials Science and Engineering)

TITLE: The Effect of Post Processing on the Mechanical Properties and Fracture Mechanisms of AlSi10Mg Produced Through Selective Laser melting

AUTHOR: Youssef Salib, B.Eng (McMaster University

SUPERVISOR: Dr. David Wilkinson

PAGES: xi, 69

Abstract

The use of selective laser melting for AlSi10Mg has been gaining a lot of popularity, but unfortunately, there are a great deal of issues surrounding internal porosity. Hot isostatic pressing (HIP) has been used in many instances alongside a standard T6 treatment to reduce porosity, but that typically involves water quenching. The application for this project is meant for the satellite industry, which has tight dimensional tolerances and as such, water quenching is not adequate. Currently, annealing for a stress relief treatment is the only post-processing measure that does not involve water quenching. This project studied a novel direct HIP approach, whereby an argon quench is used after solution annealing. Three different cooling rates were studied within the DHIP process (DHIP-L=50°C/min, DHIP-M=200°C/min, and DHIP-H=400°C/min) and compared to specimens that were stress relieved (SR). Uniaxial tensile testing revealed that the strength and ductility of DHIP-H outperformed the SR condition. The true stress/strain results showed that all DHIP conditions had a superior true strain and true stress at fracture. All DHIP conditions and SR showed evidence of void growth and coalescence. SR fracture is driven through crack initiation, while the DHIP conditions fracture is driven through localized necking. In-situ tensile tests via scanning electron microscopy coupled with μ-DIC revealed that the DHIP conditions feature damage due to particle fracture, while the SR condition experiences strain localization along the interface of Si particles and the α-Al phase. In-situ tensile testing via XCT studied a comparative analysis between DHIP-M and SR and revealed that DHIP-M experiences more void growth and nucleation than the SR condition.

Acknowledgements

First and foremost, I would like to express my gratitude to Dr. David Wilkinson and Dr. Hatem Zurob for overseeing this project. Their guidance and wisdom has been of upmost importance for the completion of this thesis.

I would also like to express my gratitude to Burloak Technologies for their partnership and funding for this project. The guidance from Hamid Azizi and Paul Tallon from Burloak Technologies has been extremely valuable for the completion of this thesis.

Although this project was completed, there were many ups and downs, but my family was always there to support me throughout the process. My loving mother Rania Andrawos, my dear brother Karim Salib, and my lovely little sister Zoe Salib have always stood by my side throughout the entirety of my education.

My fantastic friends, Yuki Ando, Ibrahim Waseem, Hamza Waseem, Abdullah Waseem, Santiago Parra Guzman, Sean Do, Miriam Ghaly, Gabrielle Ghaly, Talha Aziz, Joshua Salem, and Joshua Halim for always having my back when I needed it most throughout my education.

Lastly, the members of the Center for Automotive Materials and Corrosion have offered a great source of mentorship. In particular, I would like to express my gratitude to Dr. Elizabeth McNally and Moisei Bruhis for all of their support in the laboratory facilities, as well as Concetta Pelligra and Cal Siemens for their support with training and data analysis.

Table of Contents

Table of Figures

List of Tables

List of Symbols and Abbreviations

DHIP	Direct Hot Isostatic Pressing
DIC	Digital Image Correlation
EDM	Electrical Discharge Machining
GP	Guinier Preston
h	Hatch Spacing
HAZ	Heat Affected Zone
HIP	Hot Isostatic Pressing
P	Laser Power
SEM	Scanning Electron Microscopy
SLM	Selective Laser Melting
SR	Stress Relieved
t	Layer Thickness
UTS	Ultimate Tensile Strength
V	Scan Speed
VED	Volumetric Energy Density
XCT	X-Ray Computed Tomography
μ-DIC	Micro – Digital Image Correlation

1.0.0 Introduction

The use of additive manufacturing can enable components with complex geometry and light weight, making the process very suitable for aerospace applications. Amongst lightweight alloys of adequate mechanical properties, AlSi10Mg is among the most popular. Though selective laser melting (SLM) offers the potential to produce components of high strength and complex geometry, the ductility is not adequate, therefore it is imperative to heat treat the material to achieve a good balance between strength and ductility. As a result of the SLM process, internal porosity is still present, with many of the pores acting as stress concentrators. This poses an issue for early failure under loading, and as a result, it is imperative to mitigate these defects. To battle these defects, it is important to use hot isostatic pressing (HIP).

Currently, Burloak technologies employs a post-processing measure that contains the following steps:

1. Annealing for stress relief (T=300°C, t=120 min)
2. Hot isostatic pressing (T=510°C, P=101.7 MPa, t=180 min)
3. Solution annealing (T=510°C, t=360 min) followed by a water quench
4. Artificial aging (T=170°C, t=300 min)

Although the final mechanical property results achieved are desirable, the solution annealing stage entails water quenching, which introduces part distortion. Therefore, the only viable post-processing measure for low part distortion entails only a stress relieving step (T=300°C, t=120 min). The satellite industry has tight dimensional tolerances for its components, and thus, a post-processing measure that not only reduces porosity, but also

increases ductility and strength is desirable. Therefore, the proposed idea is as follows (This process will be known as DHIP in this thesis, representing direct HIP):

1. Hot isostatic pressing (T=530°C, P=101.7 MPa, t=30min)
2. Artificial aging (T=170°C, t=300 min)

This approach will utilize a solution annealing temperature, which will enable the microstructure to coarsen, while stress relieving at the same time (since the solution annealing temperature is well above the stress relieving temperature). It is important to note that a controlled argon quench is used, therefore decreasing the susceptibility to part distortion in comparison to a standard water quench. In theory, superior mechanical properties should be achieved, while closing internal porosities (when comparing to the as-stress relieved condition).

The objective of this research is to understand the process-structure-property relationship for AlSi10Mg produced through SLM that underwent the following post processing measures:

1. Annealing for stress relief at T=300°C and t=120 min (known as SR)
2. DHIP using 50°C/min quench rate (known as DHIP-L)
3. DHIP using 200°C/min quench rate (known as DHIP-M)
4. DHIP using 400°C/min quench rate (known as DHIP-H)

Cooling rates are being studied to understand the quench capabilities of the HIP vessel to ensure adequate mechanical properties. These conditions will be studied using uniaxial tensile testing, in-situ tensile testing via SEM coupled with μ-digital image correlation (μ-DIC), and in-situ tensile testing via x-ray computed tomography (XCT).

2.0.0 Literature Review

2.1.0 Selective Laser Melting (SLM)

In recent years, additive manufacturing has been gaining a high degree of attention, because of the complex geometries that can be created which otherwise cannot be achieved through traditional manufacturing methods. SLM is a manufacturing technique with the ability to manufacture components by consolidating powder particles using a laser beam, through a layer by layer approach [1]. The apparatus works through the deposition of powder upon a build plate, whereby a high-power laser melts the first layer of the component selectively. The build plate is then lowered by the distance equivalent to the layer thickness, after which more powder is deposited over the previously built layer. The laser will then selectively melt the next layer, and this process will keep repeating itself until the component of interest is created. A diagram illustrating this process can be found in Figure 1 [2].

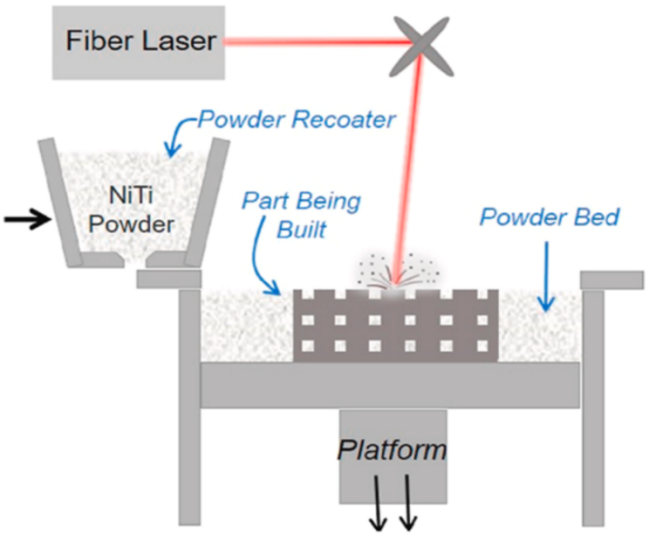

Figure 1: An illustration of the SLM process [2]

When melting powder metal using a high-power laser, the introduction of high rates of heating and cooling rates is to be expected. This will produce metallic components of exceptional strength due to the resultant refined microstructure [3]. As a result of the high strength achieved, the ductility will naturally suffer as a consequence due to the increased defect density and residual stresses present in the microstructure due to the high cooling rates [1]. Furthermore, the use of a high energy laser in this context will introduce microstructural heterogeneities along each laser pass. These regions are known as melt pools and their boundaries are known as melt pool boundaries [4]. This is visually shown in figure 2 (the laser would be scanning in and out of the page).

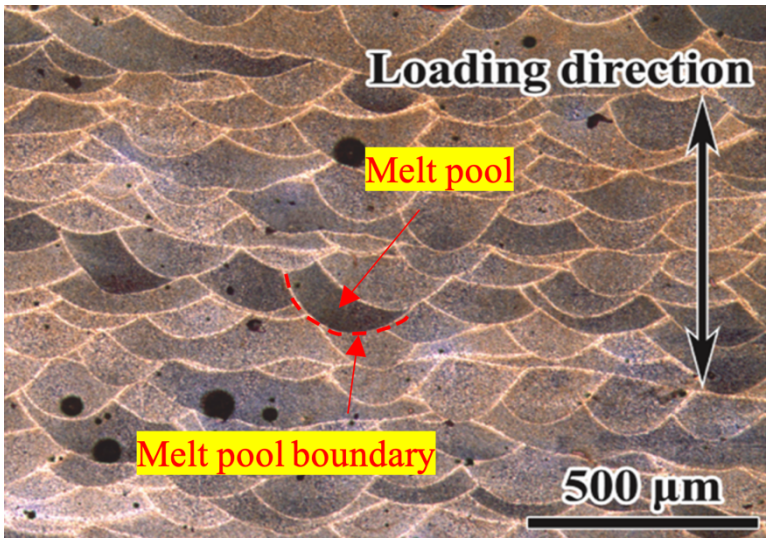

Figure 2: Micrograph of as-built AlSi10Mg depicting the presence of melt pools [4]

Densification in a component produced through SLM can reach high levels of approximately 99.9%. Although there is a high density, the limited porosity within a component produced through SLM can still be determinantal to mechanical properties. Two main types of pores are recognized: gas pores or metallurgical pores, and lack-of-

fusion pores. Metallurgical pores are small and spherical in shape and are on the order of tens of microns in size. They form from the presence of moisture on the powder's surface before manufacturing. The trapped moisture causes the formation of gas pores during SLM, and at high temperatures, causes the gas to reach high pressures, and thus producing the pore. The morphology of these metallurgical pores is typically spherical, and they do not pose any major stress concentrators within the component. On the other hand, "lack-of-fusion pores" (also known as keyhole pores) occur when some powder does not completely melt during the manufacturing process, resulting in irregularly shaped and larger pores. The irregular morphology introduced by the lack of fusion pores creates a problem as it may contain stress concentrators, which is a leading cause of early failure in materials produced through SLM [5]. Examples of both porosity forms can be observed in Figure 3.

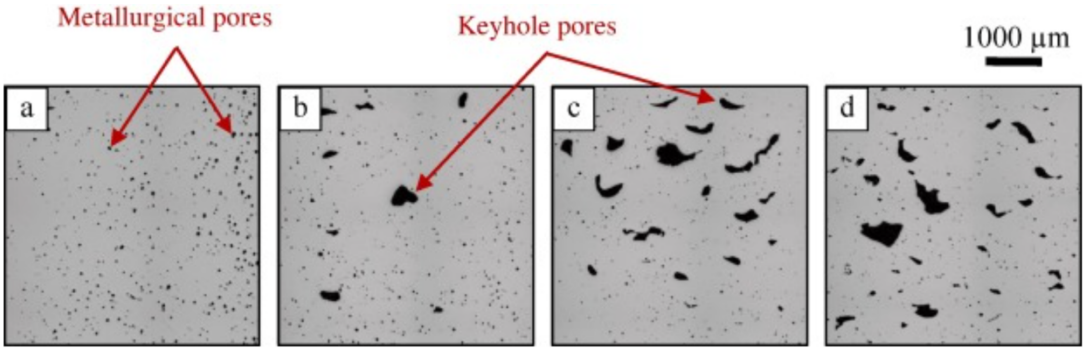

Figure 3: Micrographs showing examples of metallurgical pores and lack-of-fusion pores (also known as keyhole pores) [5]

Metallurgical pores are unavoidable for the most part because they are due to the pre-present moisture from when the powder was manufactured. Therefore, to lessen the presence of these metallurgical pores, it is imperative that the supplied powder comes from a high-quality source. On the other hand, the lack-of-fusion pores can be mitigated through

optimizing the printing parameters, which is associated with optimizing the amount of energy per unit volume in the component during the SLM process. The processing parameters associated with SLM are laser power (P), layer thickness (t), scan speed (v), and hatch spacing (h), and they can all be related to the volumetric energy density (VED):

$$VED = \frac{P}{vht} \quad (1)$$

The lack of optimization of the volumetric energy density will lead to poor mechanical performance, a higher density and size of lack-of-fusion pores, and a non-desirable microstructure [6], [7].

Even after an optimized volumetric energy density is achieved, metallurgical pores and lack-of-fusion will still be present, but at a much smaller frequency than with an unoptimized volumetric energy density. Therefore, another measure must be employed to ensure maximum part quality with respect to porosity. The implementation of hot isostatic pressing (HIP) is used to reduce the porosity and has been gaining popularity in the additive manufacturing industry, especially with light metals. This process is able to provide the necessary heat treatment required and simultaneously provide a high pressure environment, therefore substantially reducing interior defects of components produced through SLM, while providing a homogenized microstructure, which leads to superior mechanical properties, specifically, ductility [8].

2.2.0 AlSi10Mg

The material of interest in this project is AlSi10Mg, a popular aluminum alloy used in the aerospace industry for its light weight and good mechanical properties. This alloy is

known to typically have approximately 10wt% Si, 0.35wt% Mg, and a small amount of Fe, with the balance being Al [8], [9], [10].

Fast heating and cooling rates are introduced during SLM as mentioned previously, hence it is anticipated that the components made using this technique will have a fine grain structure. As a result, the aluminium matrix contains a fine network of Si particles, and the eutectic silicon phase is substantially smaller than its cast equivalent. The α-Al phase, the Si rich phase (eutectic silicon), will be the two phases present, as Mg_2Si precipitates (in the as-built state). The tensile strength of the components produced using this process is anticipated to be significantly higher than that of its cast counterpart due to the nature of the microstructure, which is extremely fine. The resultant microstructure yields a high volume of grain boundaries which impedes dislocation movement, thereby enhancing the mechanical performance of parts produced through SLM [10]. Figure 4 shows a phase diagram describing the key elements (Al and Si) for this system [11].

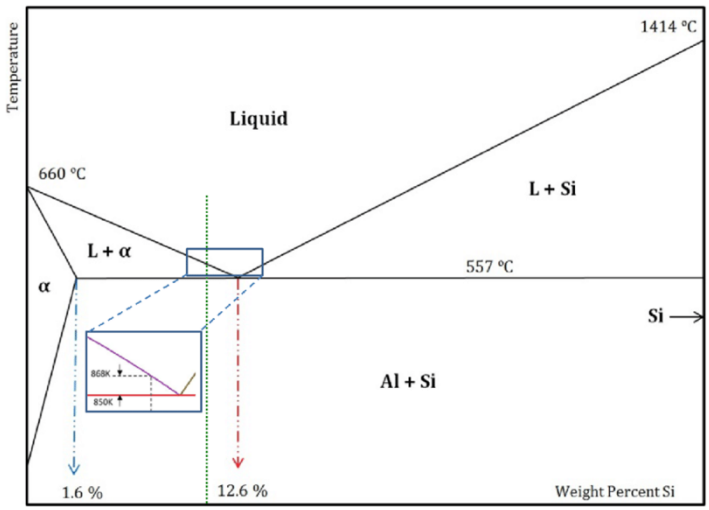

Figure 4: A phase diagram of the Aluminum-Silicon system [11]

2.2.1 Post Processing of AlSi10Mg

In this research, two main post processing techniques will be studied. The first is the stress relief (SR), which entails annealing at 300°C for 2 hours with the goal of removing residual stresses in the component. The second is a DHIP treatment, which entails solution annealing at 530°C for 30 minutes (in the HIP vessel using P=101.7MPa), followed by artificial aging at 170°C for 5 hours.

Microstructurally, the SR condition will exhibit finely distributed Si particles within the α-Al phase, which is indicative of Si supersaturation in the α-Al matrix of the as-built condition. The SR condition will also feature coarsening in the pre-existing Si particles [12]. Furthermore, any work hardening caused by the heating and cooling from the laser during the SLM process (due to thermal expansion) is relieved, and any residual stresses are therefore reduced substantially [13]. However, with respect to the DHIP treatment, this process involves annealing temperatures above the recrystallization temperature, along with an elevated pressure, followed by artificial aging. Microstructurally, this will result in a higher densification due to the elevated pressure, therefore, the density of pores will be much less than that of the stress relieved condition. Furthermore, there is further coarsening of the Si particles in comparison to the SR condition, and the formation of a stable intermetallic phase. The elevated temperature also promotes the precipitation of Mg_2Si, which allows for age hardening to take place when exposed to lower temperatures [12]. The differences microstructurally between the as-built state and annealing at 300°C and 530°C, are schematically represented in Figure 5.

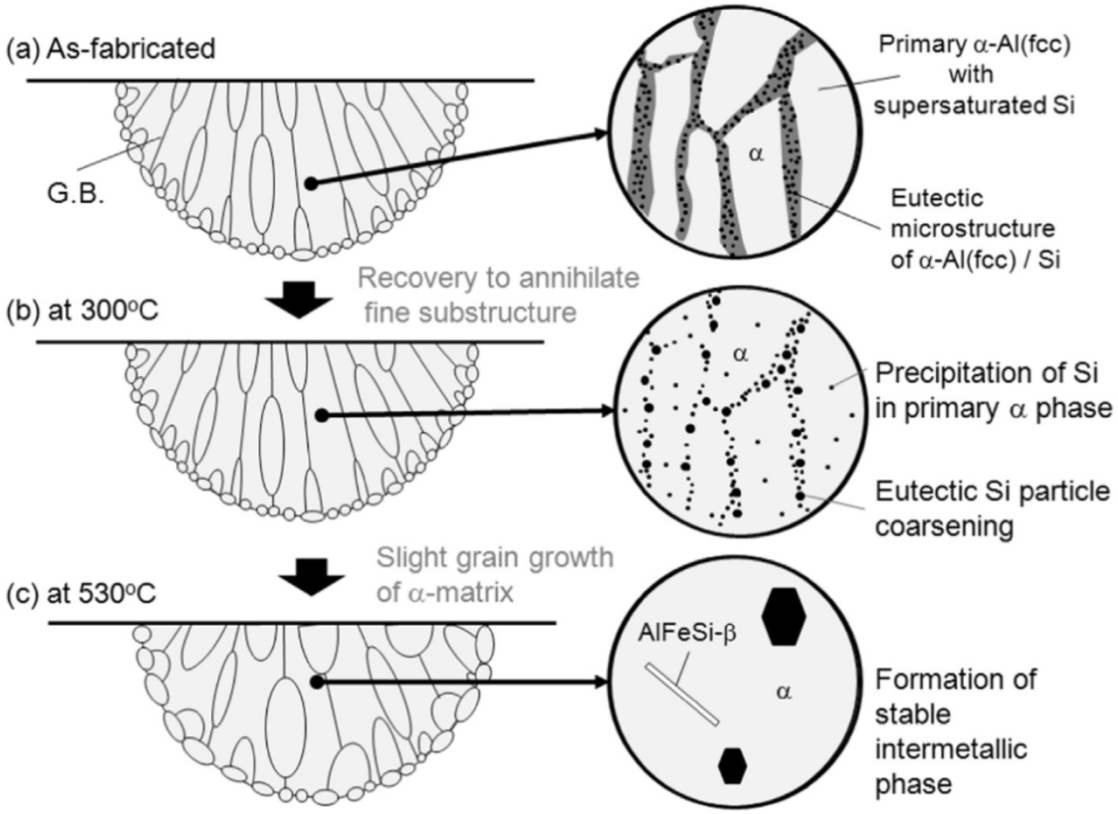

Figure 5: A visual representation of the microstructure of AlSi10Mg in the as-built state (a), at 300°C annealing state (b), and at 530°C annealing state (c) [12].

2.2.2 Precipitation Formation and Precipitation Coherency Effects

The most important precipitate in an Al-Si-Mg system is magnesium silicide (Mg_2Si). The process of SLM entails high cooling rates, and thus, it can be expected that a supersaturated solid solution is achieved. The process of Mg_2Si precipitation starts through the formation of a Guinier-Preston zone (GP zone), which is on the scale of approximately 10nm, featuring a needle-shaped morphology. When the process of artificial aging begins, the GP zones will start to dissolve and form particles of homogeneous β"-Mg_2Si, which nucleate uniformly in the lattice. In this case, a high degree of coherency is achieved,

therefore, coherency-strain fields are developed, leading to an increase in strength of the alloy. As aging progresses further, β"-Mg_2Si will transition to a heterogenous β'-Mg_2Si, and the more β'-Mg_2Si grows, coherency will begin to decrease, therefore a reduction in lattice distortion will be achieved and therefore, a decrease in strength will be observed due to the decreased coherency. If the β'-Mg_2Si precipitate is aged further, equilibrium β-Mg_2Si will be achieved in a rod or plate-shaped morphology. Equilibrium particles will be completely incoherent with the matrix, and will feature a large size and coarse distribution, which will produce an even further reduction in strength [14].

2.3.0 Mechanical Properties of SLM AlSi10Mg under Different Post-Processing Conditions

A decent amount of research has been conducted surrounding the mechanical properties of AlSi10Mg produced through SLM. This section will cover studies conducted on AlSi10Mg which have experienced an SR treatment and SR+HIP treatment in literature.

A study conducted by Ertugrul et al [15], was able to study the effect of HIP and heat treatment on the mechanical properties of AlSi10Mg produced through SLM. In this study, cylindrical specimens were used, and all the samples were built in the horizontal direction with respect to the build plate. The study observed the mechanical properties of AlSi10Mg that underwent a SR treatment, and it compared SR with the addition of HIP. The SR treatment was conducted at 300°C for 2 hours, and the HIP treatment was conducted at 500°C for 75 minutes in an argon atmosphere at 100 MPa, with a quench rate of 50°C/min. It was observed that the SR samples experienced a yield strength of 210 ± 16 MPa, with a UTS of 302 ± 15 MPa, and a strain to failure of 10.7 ± 1.6%. The SR with HIP applied subsequently, showed a yield strength of 108 ± 3 MPa, a UTS of 176 ± 1 MPa, and

a strain of 25.0 ± 0.5%. There was no artificial aging applied to the SR+HIP condition, and the Si phase had time to coarsen, hence the substantial decrease in strength.

Finfrock et al [16] conducted a similar study, whereby a comparison of the mechanical properties was made between specimens that underwent SR (300°C for 2hrs) and samples that underwent SR followed by HIP (521°C for 2 hours with a pressure of 103 MPa). It was reported that specimens that underwent the SR treatment had a UTS of approximately 170MPa, and a strain of about 7%. The SR with subsequent HIP experienced a strength reduction of about 100MPa in comparison to the SR specimen with a strain of about 28%.

It should be noted that many other studies have been conducted on AlSi10Mg that experienced SR followed by HIP, but not many, if any, showed the effect of directly using the HIP to combine the stress relieving, solution annealing, in conjunction with HIP, then following up with artificial aging. This is one area that this research aims to shed light on.

2.3.1 Mechanical Properties of Alternative Aluminum Alloys

This section will compare popular aluminum alloys used in the aerospace industry, in particular, AA6061 that underwent T6 treatment (AA6061-T6), and A359. These two alloys were chosen because, SLM AlSi10Mg aims to be a viable alternative to these alloys.

According to the ASM handbook on aluminum alloys, AA6061-T6 features an ultimate tensile strength of 310 MPa, a yield of 275 MPa, and an elongation of 12% [17]. Radhakrishan et al [18] reported in a study pertaining to the mechanical properties of AA6061-T6, that their observed ultimate tensile strength was 328 MPa, the yield strength was 276 MPa, and the elongation was 12%. A359 that underwent a T6 treatment typically

has an ultimate tensile strength of 345 MPa, a yield strength of 290 MPa, and an elongation of 5.5% [17].

2.4.0 In-situ Tensile Testing Techniques

Two in-situ (or continuous) tensile techniques are used in this research. The first is known as in-situ tensile testing via scanning electron microscopy (SEM) coupled with micro digital image correlation (μ-DIC). The second is known as in-situ tensile testing via x-ray computed μ-tomography (μ-XCT). Both techniques involve a tensile test which is conducted in an interrupted fashion, therefore revealing key details on the behavior in which the material deforms.

2.4.1 In-situ Tensile Testing via SEM coupled with μ-DIC

2D DIC is a commonly used technique to measure strain through the identification and tracking of features on the surface of the specimen subjected to loading. Typically, a stochastic speckle pattern is applied to the surface of a macro scale tensile specimen and a camera will take multiple images of the sample neck to track the movement of the speckle pattern [19]. This is known as macro DIC. A similar idea can be applied on the micro scale. A small-scale tensile jig can apply a uniaxial tensile load to a small-scale tensile coupon which has been prepared through metallography. Instead of imaging using a camera on the macro scale, in this case, the images are taken in an SEM to measure the strain on the microstructural level, therefore, giving information on how phases deform in a qualitative and quantitative manner [20][21].

Instances where the use of this technique is applied to SLM AlSi10Mg is not common. One of those was conducted by Zou et al [22], whereby they enhanced the tensile

ductility of as-built SLM AlSi10Mg by reducing the density of melt pool boundaries through altering the hatch spacing printing parameter. This was quantified through the use of local DIC (μ-DIC) along the melt pool boundary to study the different hatch spacing values used during SLM. Another instance studied the effect of voids and microstructure on the deformation of SLM AlSi10Mg in the as-built condition. This study lacked the use of μ-DIC, the tests were mainly used to observe voids and microstructural features during deformation [3]. Therefore, there is a clear gap in the research pertaining to studying different heat treatment conditions with respect to the use of in-situ tensile testing coupled with μ-DIC.

2.4.2 In-situ Tensile Testing via X-ray Computed μ-Tomography (XCT)

In-situ tensile testing via XCT is a 3D technique that will provide deformation behavior information as a function of true strain. This test is typically used to understand void growth, nucleation, along with damage accumulation.

A study conducted by Samei et al. [23] observed the evolution of pores during deformation of as-built AlSi10Mg. This was accomplished through an interrupted tensile test within the XCT, yielding 5 steps of deformation. It was reported that the pore volume fraction increased in an exponential matter, and that the mean diameter increased as the true strain increases (their associated graphs can be seen in figure 6).

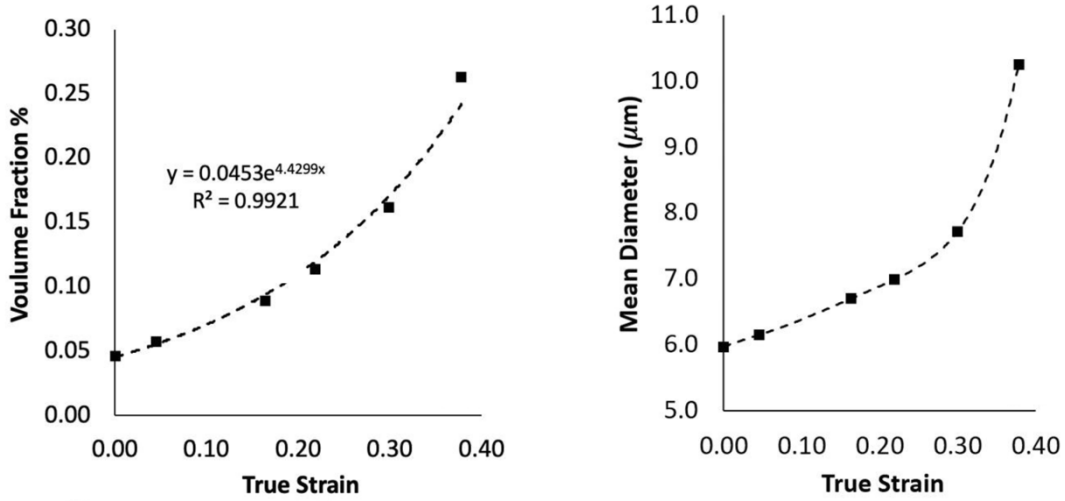

Figure 6: Graphs representing the Volume fraction % as a function of true strain (left) and mean diameter as a function of true strain (right) [23]

A research gap is presented through the lack of work being done in the effect of HIP using this technique. No records were found using in-situ tensile testing via XCT to study samples of AlSi10Mg that experienced a HIP treatment.

2.5.0 Previous Work

In conjunction with the work presented in this thesis, prior work was accomplished by Salib [24] at McMaster university in 2020-2021. The objective of this work was to characterize the mechanical properties of AlSi10Mg in the as-built state, and to observe the microstructural deformation mechanisms. This was mainly accomplished using uniaxial tensile testing and in-situ tensile testing via SEM coupled with μ-DIC. A full microstructural characterization was accomplished through secondary electron imaging of the microstructure in the different build orientations to better understand the microstructure, and any present defects from the as-built state. Lastly, an understanding of the thermal history was achieved using hardness testing along the build direction.

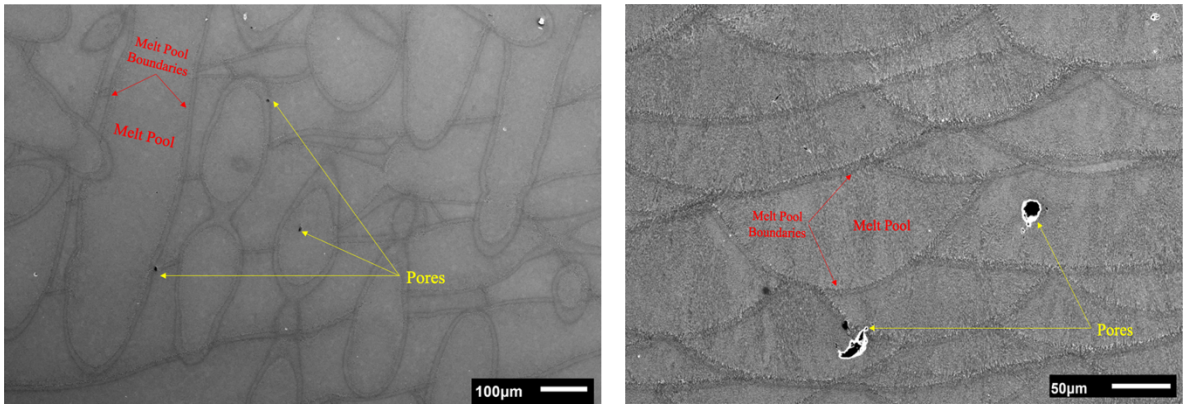

Figure 7: Secondary electron images of as-built AlSi10Mg in the direction perpendicular to the build direction (left) and the direction parallel to the build direction (right)

It was briefly mentioned in section 3.1.0 that melt pools and melt pool boundaries are a natural occurrence of any material produced through SLM. Micrographs of the as-built state show this in figure 7. Pores were clearly present in the microstructure as shown in both micrographs. It was also observed that there is a microstructural heterogeneity mainly along the melt pool boundaries. This is clearly shown in figure 8, whereby two distinct regions are shown along the melt pool boundary. The first region is the remelted

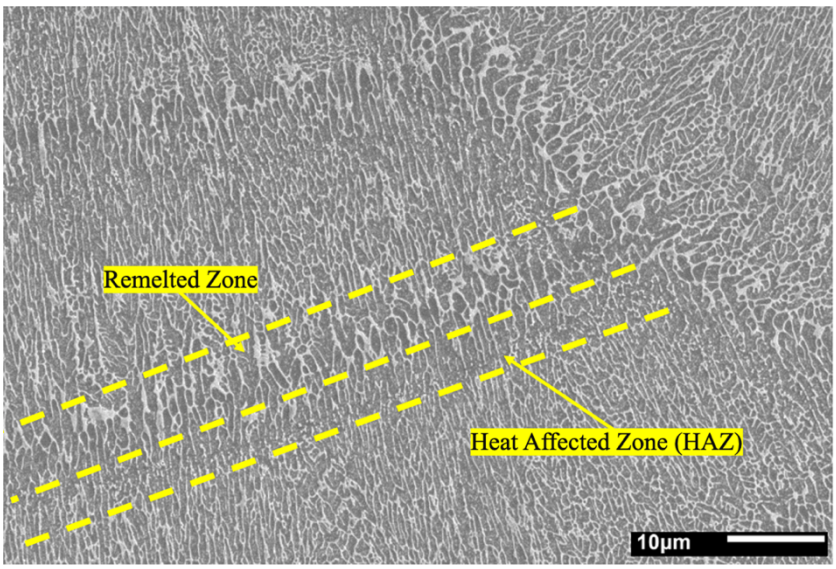

Figure 8: Micrograph taken along melt pool boundaries indicating the presence of the remelted zone and the heat affected zone (HAZ).

zone, and it is formed because of residual heat remelting a portion of a previously existing adjacent melt pool. The second region is known as the heat affected zone (HAZ), which is hypothesized to be as result of residual heat that did not reach the melting temperature, yet allowed for thermal expansion and contraction, therefore yielding decoherence in the Si phase.

A strong interest came of this observation during the in-situ tensile testing via SEM experiments. The μ-DIC results on the scale of the melt pool boundaries showed that the strain localizes almost exclusively along the melt pool boundary, specifically along the heat affected zone (as shown in figure 9). It was also observed that cracks initiate and propagate along the melt pool boundary. This was confirmed through observing the microstructure near the fracture tip, and through observing the fracture tip through fractography. This was

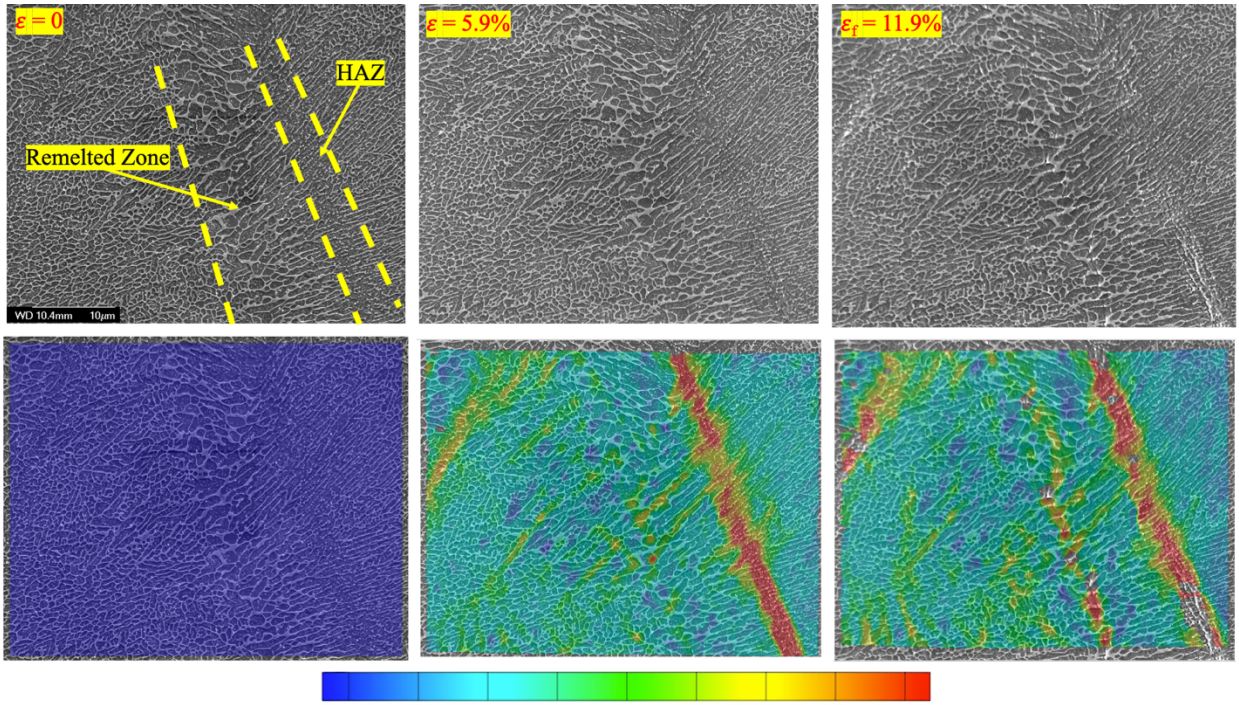

Figure 9: In-situ tensile test with their associated μ-DIC maps at x2500 magnification. The strain range is shown with the bar on the bottom, where blue regions feature low strain and red regions feature high strain

also coupled with an x-ray μ-computed tomography scan to show this behavior. All three of these observations are shown in figure 10. The fracture surface on the right shows a crack that is on the scale of a melt pool boundary, which was hypothesized to be caused at the heat affected zone. Microstructurally, a crack formed along the heat affected zone. The 3D XCT model revealed many regions along the edge of the fracture surface that were on the same scale as melt pools, therefore indicating that much of the fracture is driven by the melt pool boundary.

Uniaxial tensile testing showed that the as-built condition shows exceptional strength, yet a lack in ductility, which was to be expected and was in-line with various sources. During tensile testing, it was observed that fracture exclusively occurred near the tensile sample shoulders. This behavior was indicative of a mechanical property heterogeneity in the material, and as such, a hardness investigation as a function of the

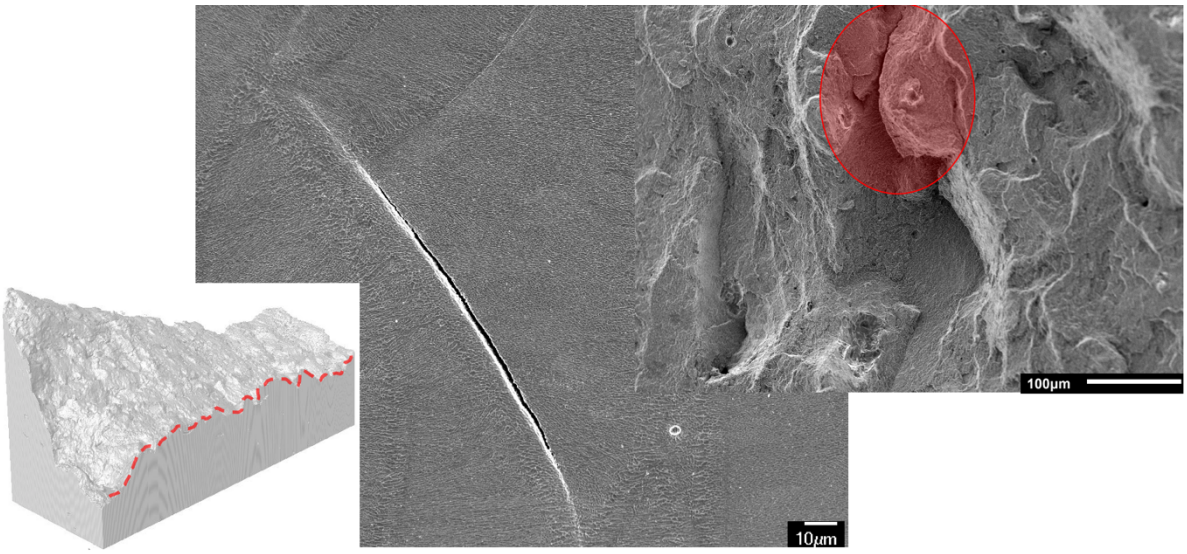

Figure 10: A micrograph of a crack forming along the melt pool boundary near the fracture tip (middle) along with an image of the fracture surface highlighting a region on the scale of a melt pool boundary (right), and a 3D XCT model showing features along the fracture tip that are on the scale of melt pools (left)

distance from the first layer formed during SLM was completed. Hardness points were taken along the build direction to understand if there were any mechanical property heterogeneities. Figure 11 shows the hardness data, indicating that the hardness increases as the distance from the first layer formed during SLM increases. This is attributed to the thermal history associated with the material, whereby the baseplate is heated at 200°C, therefore the layers closest to the build plate were experiencing a constant temperature throughout the whole build. Due to the nature of SLM, any layers of a component built through SLM that are close to the build plate will experience different mechanical properties, thus indicating that the orientation of a component built during SLM is imperative with respect to mechanical properties.

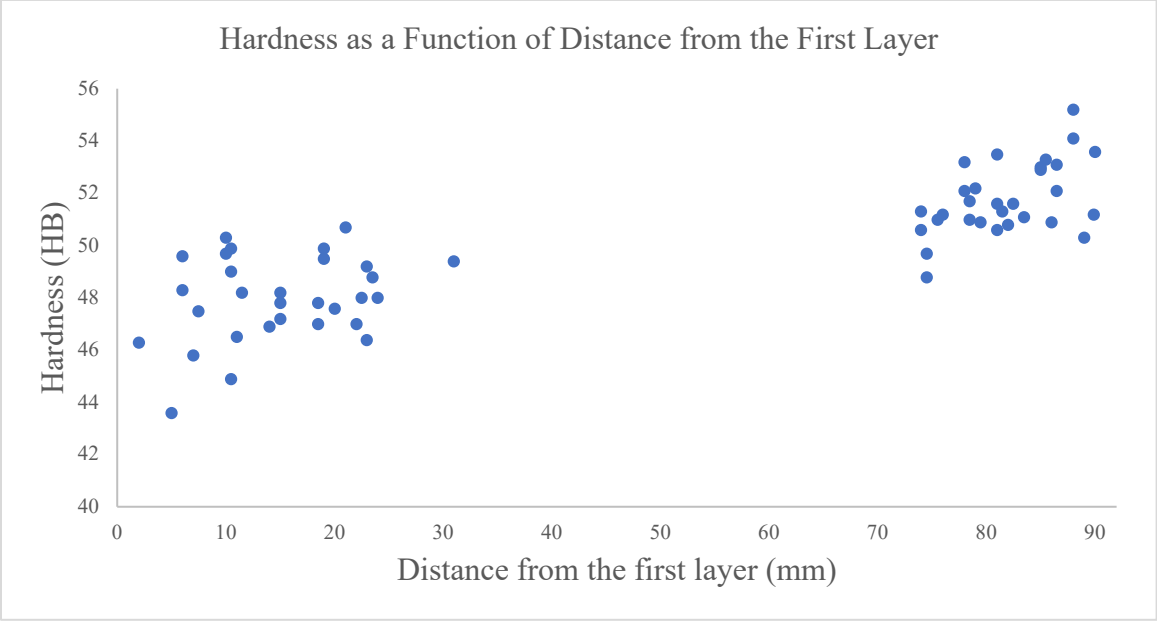

Figure 11: Hardness as a function of the first layer formed during SLM (note, there are points missing in the center because a tensile sample was used, and points were taken exclusively at the sample shoulders, due to a shortage of material)

3.0.0 Research Objectives

The objective of this research is to develop a direct HIP process that enhances the strength and ductility of the baseline stress relieved approach. A comparative analysis of the post processing conditions; SR, DHIP-L, DHIP-M, and DHIP-H will be studied through the use of uniaxial tensile testing, in-situ tensile testing via SEM, and in-situ tensile testing via XCT. This comparative analysis aims to understand the following research objectives:

1. Optimization of the cooling rate during the direct HIP process
2. Delineating the effect of post-processing on the mechanical properties of AlSi10Mg
3. Understanding the fracture mechanisms microstructurally as a function of post-processing conditions
4. Understanding the void growth and nucleation behaviour between processing conditions

Understanding these points will lead to a deeper understanding of the process-structure-property relationship of SLM AlSi10Mg subject to various post-processing conditions.

4.0.0 Experimental

Sample Preparation for Metallography

Samples that were prepared for metallography were cold mounted with epoxy and hardener. After the sample is cured, the sample was ground using 320 grit SiC paper for approximately 1 minute, followed by 9µm diamond suspension on the Struers MD Dac pad, 3µm diamond suspension on the Struers MD Mol pad, and OP-U on the Struers MD Chem pad. In order to reveal the microstructure, it was found that Keller's reagent (1% HF) was adequate. Etching takes approximately 2-4 seconds depending on the surface area of the specimen.

Scanning Electron Microscopy (Secondary Electron Imaging)

The JOEL 7000-F and the JOEL 6610 were both used to image the microstructure of the sample. The JOEL 6610 was used when fractography was being employed, or when microstructural images did not need to exceed x3000 magnification. If any microstructural images needed to be taken further than x3000 magnification, it was found that the JOEL 7000-F produced much higher quality images. Since this material exhibits a small grain size, the JOEL 7000-F was used often to image the microstructure at high magnifications.

4.1.0 Heat Treatment Study

4.1.1 Homogenization Study

Cube specimens were additively manufactured at Burloak technologies having the dimensions of 12.7mm x 12.7mm x 12.7mm. These specimens were heat treated using a tube furnace to study the homogenization holding time. EOS, the company that produced the selective laser melting machine, recommended that the temperature for homogenization

for AlSi10Mg should be 530°C [25]. However, the holding time was to be determined. Hold times of 0.5hr, 1hr, and 2hrs were studied at 530°C.

4.1.2 Aging Study

A precision saw was used to slice the samples that were studied in the "Homogenization Study" in half. One half was kept as being only annealed at 530°C, while the other half was taken to be artificially aged. This was accomplished for all annealing hold times. These samples were then taken to the furnace to be aged at 170°C for 5 hours followed by an air cool.

4.1.3 Analysis of Homogeneity

As mentioned in the "Aging Study" section, the samples were sliced in half leaving one half in an as-annealed state, and the second half that underwent annealing and artificial aging. With holding times of 0.5 hr, 1 hr, and 2 hr, this totals 6 sample halves in total. For clarity, this is summarized in a chart in table 1. Samples 1, 2, and 3 were of interest to observe the homogeneity in the microstructure, thus, they were cold mounted, and underwent metallography to reveal the microstructure. Images of the microstructure were taken on a Keyence light optical microscope.

Table 1: Summary of heat-treated samples for the homogeneity study

Sample #	**1**	**2**	**3**	**4**	**5**	**6**
Annealing Hold Time (at 530°C)	0.5 hr	1 hr	2 hr	0.5 hr	1 hr	2 hr
Aged at 170°C?	No	No	No	Yes	Yes	Yes

In harmony with microstructural imaging, microhardness measurements were taken on each samples 1, 2, 3, 4, 5, and 6. To use this device, it was required that the samples are

mounted and polished up to 1 µm. Therefore, for these measurements, metallography took place on samples 1 through 6, except during the metallography, instead of going to the OP-U step, the samples went up to 1 µm, with no etching required. For each sample, 10 microhardness indents were taken along the build direction vertically.

4.1.4 Dilatometry

A cooling rate study was conducted to see the effect of cooling rate on the aging response and the hardness. The cooling rates of interest were 1 K/s, 3 K/s, 5 K/s, 8 K/s, 15 K/s, and 200 K/s. The use of a dilatometer was able to produce heat treatments with controlled quenching. This was completed to get a more accurate understanding of the hardness to the quench capabilities in Burloak's hot isostatic press vessel.

12 samples in total were prepared, 6 underwent only an annealing process (530°C for 30 minutes) and the remaining 6 underwent the full T6 treatment with annealing and artificial aging (170°C for 5 hours). Note that the ramp up rate was 0.33 K/s, and was constant throughout each test. In total, only 6 samples were annealed in the dilatometer with the varying quench rates. These 6 samples were then sectioned in half and the second half of each specimen went into a tube furnace at 170°C for 5 hours to receive the artificial

Table 2: Summary of dilatometry sample parameters

Sample #	**1**	**2**	**3**	**4**	**5**	**6**	**7**	**8**	**9**	**10**	**11**	**12**
Cooling Rate (K/s)	1	3	5	8	15	200	1	3	5	8	15	200
Annealed at 530°C?	Yes	Yes	Yes	Yes	Yes	Yes	Yes	Yes	Yes	Yes	Yes	Yes
Aged at 170°C?	No	No	No	No	No	No	Yes	Yes	Yes	Yes	Yes	Yes

aging treatment. For simplicity, the samples were put in a chart and can be found in table 2.

Similarly, to the "Analysis of Homogeneity" section, all these samples were cold mounted and polished up to 1μm with no etching involved. Microhardness measurements were taken for all conditions, and thus an understanding of the hardness as a function of cooling rate can be understood. A sample size of 12 indents for each sample was used.

4.2.0 Uniaxial Tensile Testing

Tensile testing was employed in a series of different studies. Throughout all the tensile testing experiments, the 10kN frame was used in the mechanical testing laboratory in CAMC using a strain rate of 1mm/min. The techniques used for measuring the strain during deformation was 2D digital image correlation system (DIC) or through an extensometer. The cross-sectional area was measured with a caliper for all tensile tests beforehand. This area value will be used to calculate the engineering stress. All tensile tests were in accordance with the ASTM E8 standard [26]. After all tests were completed, the fractured tensile coupon ends were safely stored, preserving the fracture tip.

4.2.1 Tensile Sample Geometries

Different sample geometries were used for different tests during this project. For macro scale uniaxial tensile testing, there were two geometries used. The first, is a flat subsize sample geometry and can be found in Appendix A.1. The second, is a cylindrical sample geometry and can be found in Appendix A.2.

4.2.2 Tensile Testing: Orientation Effect

To study the effect of build orientation during SLM, a comparison 3 build orientations during additive manufacturing was conducted. Cylindrical samples (Height=90mm, Diameter=17.5mm) were built vertically, horizontally, and on a 45° angle. Figure 12 illustrates the various build orientations visually.

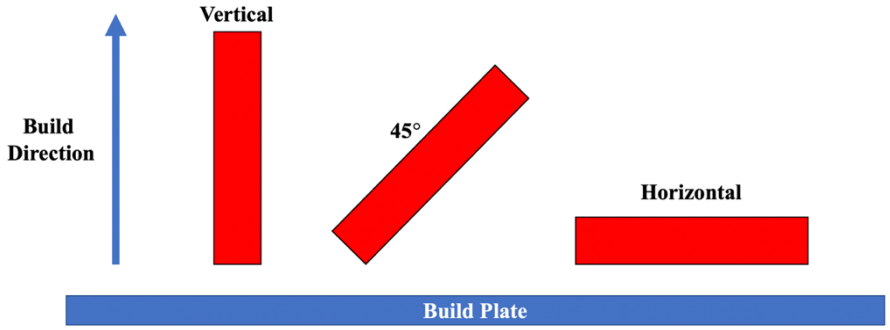

Figure 12: A visual illustration of the various build orientations studied

The cylindrical samples were then machined to produce the cylindrical tensile coupon geometry as outlined by the "Tensile Sample Geometries" section. These tests were conducted on the as-built condition, and in a stress relieved (SR) condition, entailing an annealing temperature of 300°C for 2 hours. For simplicity, table 3 summarizes all the conditions completed for the orientation effect study.

Table 3: Summary of the orientation effect tensile study coupons

Condition	Vertical	45°	Horizontal
# of As-Built Coupons	3	3	3
# of Stress Relieved Coupons	3	3	3

Digital image correlation (DIC) was used to calculate the strain during these tests. Before testing commences, the tensile coupons were lightly ground with 600 grit SiC paper. To achieve correlation with the DIC system, a stochastic speckle pattern was applied to the surface of each sample through first applying a light coat of white spray paint to the gauge length of the sample, followed by a light spray of black spray paint.

4.2.3 Tensile Testing: Homogeneity Study

A series of tensile tests were completed to confirm the mechanical properties in the samples that were heat treated to confirm the properties in an as-annealed state, and T6 condition. The sample geometry used for this series of tests was the flat subsize coupon in accordance to ASTM E8, and they were machined through electro discharge machining (EDM) out of a cylindrical coupon which was produced through selective laser melting and was received in the as-built state (vertically built). This cylindrical coupon sample geometry is the same as the coupon used in the orientation effect study.

The conditions for tensile testing were inspired by the results from the "Homogenization Study" section. Therefore, the lowest annealing time and the highest annealing time was used to study the two extremes of annealing time. Along with that, their T6 counter parts were also studied. For simplicity, the test conditions are outlined in table 4. All tensile samples were heat treated in accordance to the "Heat Treatment" section, in the same manner as the homogenization study.

Table 4: Summary of homogenization tensile testing heat treatment times

Condition #	**1**	**2**	**3**	**4**
Annealing Time (530°C)	0.5 hr	2 hr	0.5 hr	2 hr
Age Time (170°C)	0 hr	0 hr	5 hr	5 hr

Three samples were tested for each condition, therefore, with the inclusion of an as-built baseline (from Salib), a total of 15 tensile tests were completed. All tests in this section used an extensometer for strain measurements.

4.2.4 Tensile Testing: Cooling Rate Tests

A series of tensile coupons were additively manufactured vertically in the flat subsize geometry (in other words, no machining is required). These specimens were heat treated within the Quintus hot isostatic press (HIP) at Burloak Technologies. Four conditions were studied, a stress relieved condition, and three T6 conditions with varying cooling rates (defined as DHIP as per chapter 2). The T6 conditions are labelled as DHIP-L, DHIP-M, and DHIP-H, denoting, low, medium, and high cooling rates after solution annealing. The cooling rates are 50°C/min, 200°C/min, and 400°C/min respectively. A total of 12 samples were pulled (3 for each condition including SR). No grinding after the SLM process took place. The method of strain measurement was through 2D DIC.

4.3.0 In-situ Mechanical Testing Techniques

4.3.1 In-situ Tensile Testing via Scanning Electron Microscopy coupled with µ-Digital Image Correlation (µ-DIC)

This technique involves the preparation of a special micro-tensile specimen geometry that can be found in appendix A.3. Manufacturing of this specimen was through EDM of a rectangular ribbon created through SLM (vertically). The dimensions of the ribbon were a length of 120mm, thickness of 1.5mm, and a width of 10mm.

Sample preparation involved grinding the gauge length (on all sides) to achieve a uniform surface finish through the use of a 600 grit SiC paper. This is to ensure that all stress concentrators due to poor surface roughness are eliminated. The tensile specimen

was then glued using super glue over a spare sample puck. Grinding and polishing of this sample was be the same as outlined in the "Metallography" section, except it must be manual, using the spare sample puck as a grip for the micro-tensile coupon. Manual preparation was found to be the most consistent, due to the specimens being fragile. Furthermore, the micro-tensile sample holder for the auto polisher cannot be used because this alloy is not magnetic. After achieving a mirror finish, the micro-tensile specimen was placed in a glass beaker filled with acetone within the ultrasonic bath, in order to separate the tensile specimen from the puck. Once removed, fresh acetone was used to remove any residual superglue on the polished surface. The micro-tensile sample was then etched. Since the microstructure for all conditions that are of interest in this research involve a fine microstructure of alpha aluminum and silicon precipitates, to achieve a stochastic speckle pattern for μ-DIC, the deposition of colloidal silica is imperative. To do this, a spray bottle filled with OP-U was placed into the ultrasonic bath for 30 minutes to ensure that the colloidal silica particles are not agglomerated. A Struers MD Chem pad was used, and the OP-U was sprayed 1-2 times on top of the micro-tensile specimen. The specimen was then lightly rubbed on the MD Chem pad to ensure an adequate distribution of the colloidal silica particles. The sample was left to dry until there is no more liquid present on the surface of the micro-tensile sample. After the sample was dried it was cleaned with just water. The sample was then etched one more time. Lastly, using the manual microhardness machine in JHE, several indents were applied near the neck of the sample as markings to track the location of images in the SEM.

The in-situ tensile tests took place within the JEOL 7000-F, due to the requirement of having a high resolution for the fine microstructure associated with AlSi10Mg. A custom jig was created for this test and can be found in appendix A.4. The sample was placed in the jig and securely fastened in place. The jig was then placed into the chamber, then a series of trackable secondary electron images is then taken in the undeformed state. After the jig was removed from the chamber, a small force was applied (approximately a $1/8^{th}$ rotation on the bolt; see A.4 for reference). Secondary electron images were then taken at the exact same locations as before, and this process was repeated until the specimen fractures. All of the images were taken and examined in the GOM correlate software such that a strain map can be produced.

4.3.2 In-situ Tensile Testing via X-ray Computed µ-Tomography (XCT)

This technique involves the preparation of a small tensile specimen geometry that can be found in appendix A.5. Manufacturing of this specimen was through EDM of same rectangular ribbon used in 5.3.1.

The sample was prepared through grinding all the faces and edges using 600 grit followed by 1200 grit SiC paper. This was to ensure the surface is as smooth as possible, such that the surface roughness is not to be mistaken for any open pores when post-processing the data.

The tensile stage for the XCT was used, and the prepared specimen was placed inside. An initial scan in the undeformed state was taken. Initially 52kV x-rays were used, but later in the research the camera started to have defective pixels, therefore the x-ray energy was increased to 100kV. After the scan, a force was applied up to the yield point of

the specimen, after which another scan was taken to represent the yield point. This process was repeated for the points in the following areas: in-between yield and the UTS, the UTS, and after the UTS. Having at least 2 points after UTS is imperative.

All of the data was then processed using NRecon for reconstruction, CTan for analyzing 2D and 3D data of pores/voids, and CTvol for 3D model creation.

5.0.0 Results
5.1.0 Heat Treatment Study
5.1.1 Heat Treatment Study: Light Optical Microscopy

Light optical microscopy images were taken to observe the degree of homogenization as a function of time. Figure 13 shows images of samples that were annealed at 530°C for 30 minutes, 60 minutes, and 120 minutes at x1500 magnification. It can be observed that the silicon particles coarsen with annealing time.

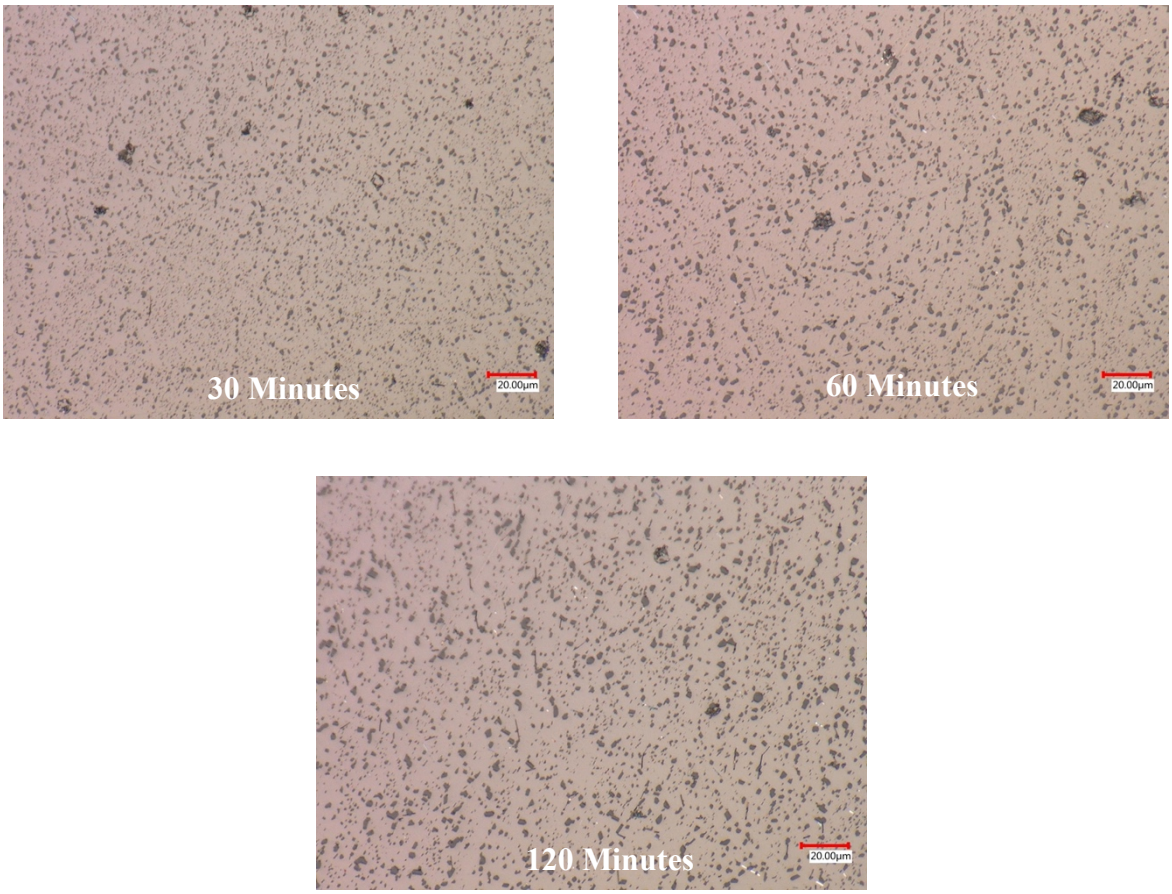

Figure 13: Micrographs of the 30 min, 60min, and 120min annealing times

5.1.2 Heat Treatment Study: Mechanical Properties

Hardness values for both annealed and artificially aged materials are shown in figure 14. The tabulated averages and standard deviations can be found in table 5. There is no significant difference of the hardness with homogenization time for both aged and annealed materials.

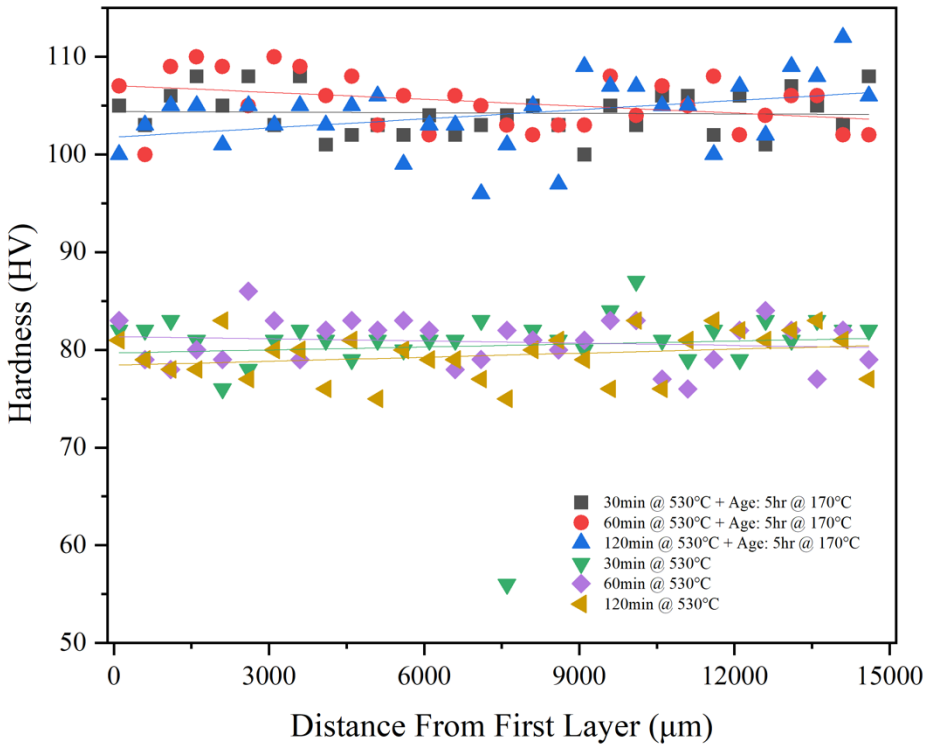

Figure 14: A scatter plot comparing the hardness at different annealing times with and without artificial aging

Table 5: Average Vickers hardness values along with the standard deviations

Condition	Average (HV)	Standard Deviation
Annealed (30 min) + 5hr Age	104	2
Annealed (60 min) + 5hr age	105	3
Annealed (120 min) + 5hr age	104	4
Annealed (30 min)	80 (81*)	5 (2*)
Annealed (60 min)	81	2
Annealed (120 min)	79	3

Tensile properties are presented in figure 15 for the 30 minute and 120-minute annealing times along with their aged counterparts. Also superimposed are the as-built properties from the previous work done by Salib et al. [24]. It is evident that all heat-treated specimens outperform the as-built condition with respect to ductility. Specimens that experienced 30 minutes of annealing time in general had a higher strength than specimens

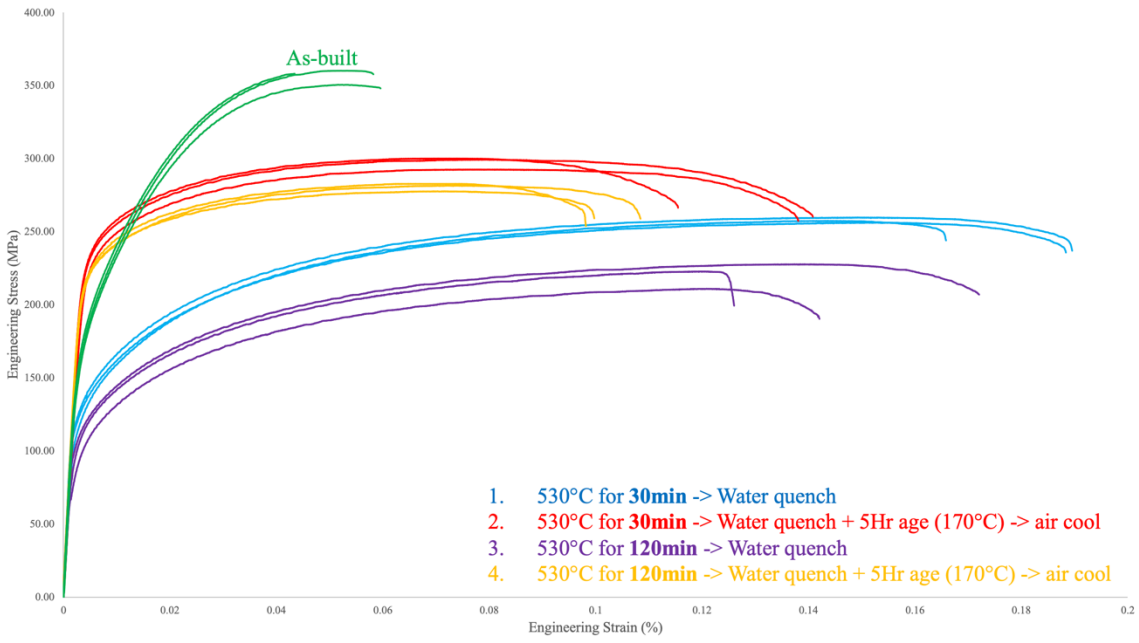

Figure 15: Engineering stress strain curves for the various annealing times with and without artificial aging

that experienced 120 minutes of annealing time, with greater ductility being evident in specimens that did not undergo artificial aging.

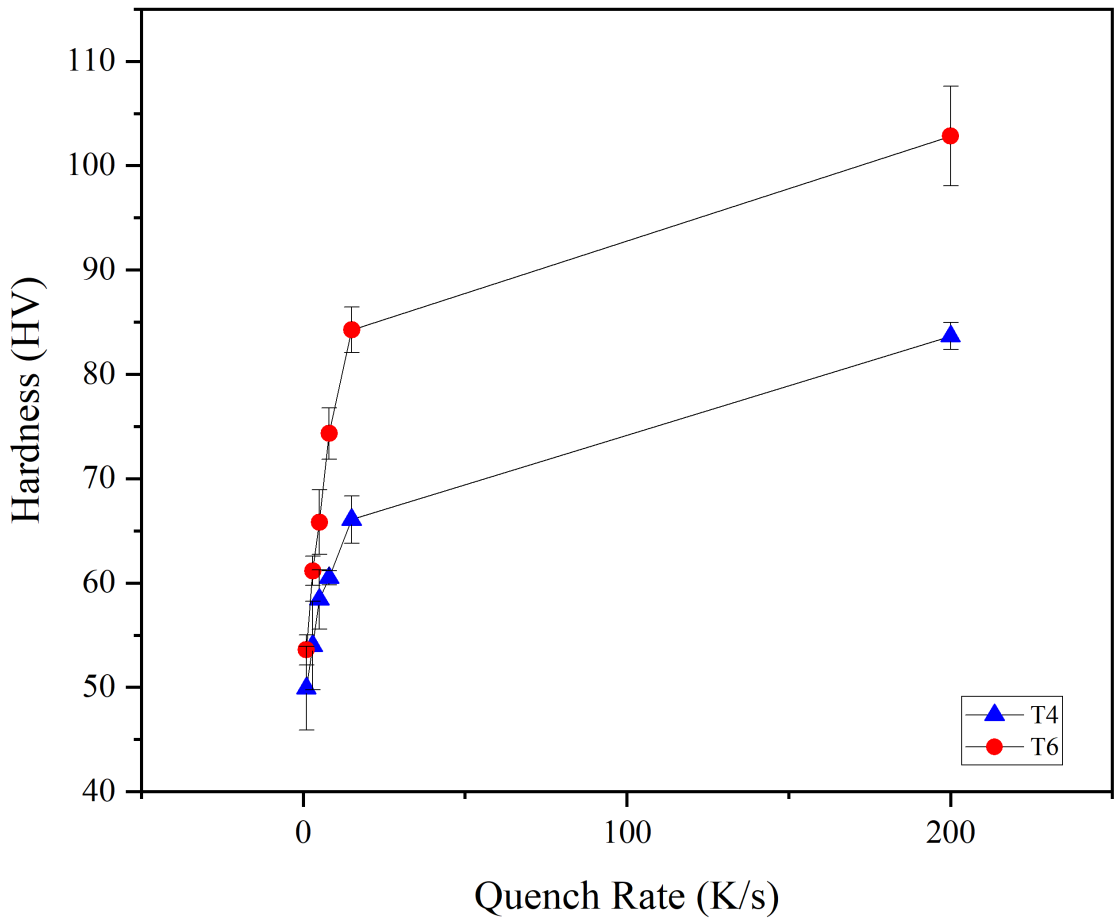

Figure 16: Hardness values for both T4 and T6 conditions under various cooling rates

Hardness values on the Vickers scale for the cooling rate study are shown in figure 16. The averages and standard deviations are shown in table 6, along with the change in hardness after aging. A general trend is seen, such that when the quench rate increases, so does the change in hardness from the T4 state to the T6 state. The change in hardness was seen to not have a significant change after 15K/s, where the change was 18.17 HV, while with the 200 K/s cooling rate the change was 19.16 HV.

Table 6: Hardness averages with standard deviations for both T4 and T6 conditions under various cooling rates

Quench Rate	**1K/s**	**3K/s**	**5K/s**	**8K/s**	**15K/s**	**200K/s**
T4 (HV)	50 ± 4	54 ± 4	58 ± 3	61 ± 1	66 ± 2	84 ± 1
T6 (HV)	54 ± 1	61 ± 1	66 ± 3	74 ± 3	84 ± 2	103 ± 5
Change in Hardness	4	**7**	**7**	**14**	**18**	**19**

5.2.0 Uniaxial Tensile Testing – Orientation Effect

As-built and stress relieved conditions both underwent tensile testing to study the effect of orientation during SLM. The engineering stress strain curves for as-built and stress relieved are shown in along with their tabulated values including the standard deviation in figure 17 and figure 18 respectively. It was observed that in the as-built condition, the values for UTS, yield strength, and elongation to fracture varied substantially. A general trend is seen that horizontally built specimens experienced the most ductility and least strength, while the vertically built specimens experienced the highest strength but least ductility. The samples built on a 45° angle had properties in the middle of both the vertical and horizontally built specimens. After annealing at 300°C to achieve a stress relieved state, it was seen that the mechanical properties were consistent across different build orientations. Although a small change in strength is evident, it was not as large as in the as-built condition.

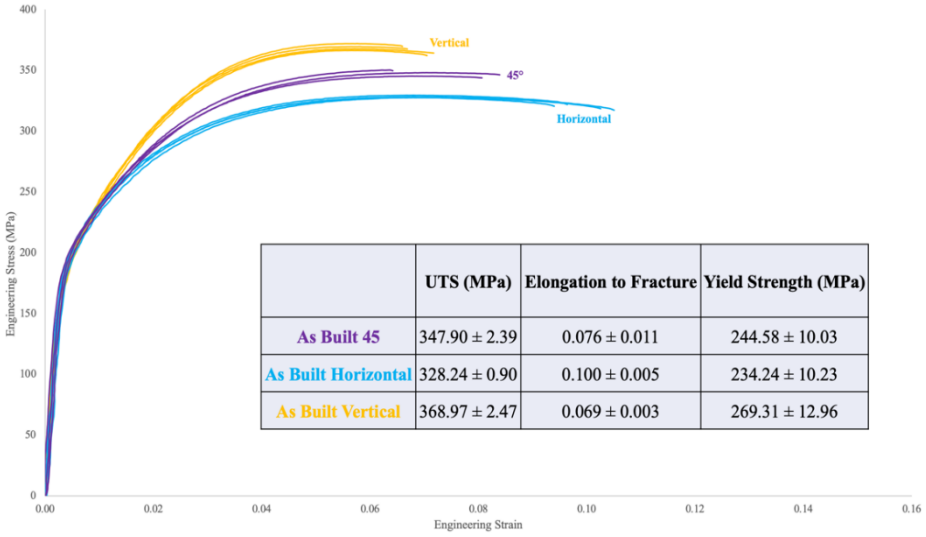

	UTS (MPa)	Elongation to Fracture	Yield Strength (MPa)
As Built 45	347.90 ± 2.39	0.076 ± 0.011	244.58 ± 10.03
As Built Horizontal	328.24 ± 0.90	0.100 ± 0.005	234.24 ± 10.23
As Built Vertical	368.97 ± 2.47	0.069 ± 0.003	269.31 ± 12.96

Figure 17: As-built engineering stress strain curves and mechanical property values

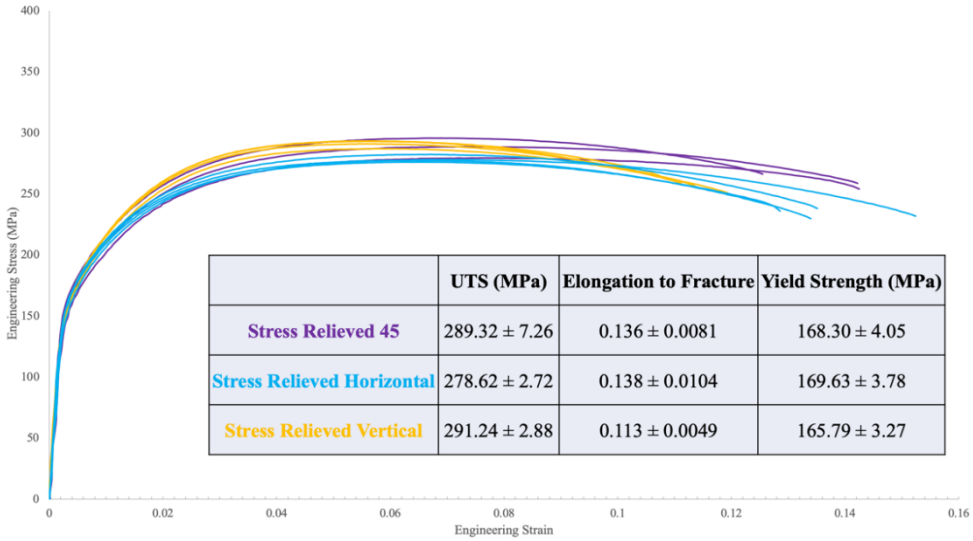

	UTS (MPa)	Elongation to Fracture	Yield Strength (MPa)
Stress Relieved 45	289.32 ± 7.26	0.136 ± 0.0081	168.30 ± 4.05
Stress Relieved Horizontal	278.62 ± 2.72	0.138 ± 0.0104	169.63 ± 3.78
Stress Relieved Vertical	291.24 ± 2.88	0.113 ± 0.0049	165.79 ± 3.27

Figure 18: Stress relieved engineering stress strain curves and mechanical property values

5.3.0 Uniaxial Tensile Testing – Effect of Cooling Rate During Direct HIP

Samples that underwent the direct HIP (DHIP) process were analyzed through uniaxial tensile testing using 2D DIC and compared to the SR condition. Figure 19 shows the engineering stress-strain curves along with the average values of UTS, yield strength,

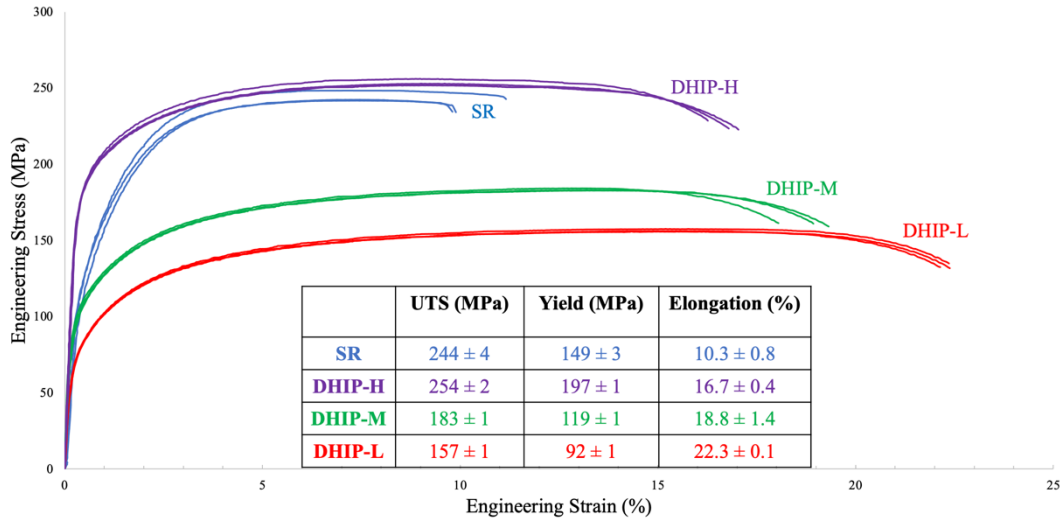

	UTS (MPa)	Yield (MPa)	Elongation (%)
SR	244 ± 4	149 ± 3	10.3 ± 0.8
DHIP-H	254 ± 2	197 ± 1	16.7 ± 0.4
DHIP-M	183 ± 1	119 ± 1	18.8 ± 1.4
DHIP-L	157 ± 1	92 ± 1	22.3 ± 0.1

Figure 19: SR and DHIP conditions engineering stress-strain curves and mechanical property values

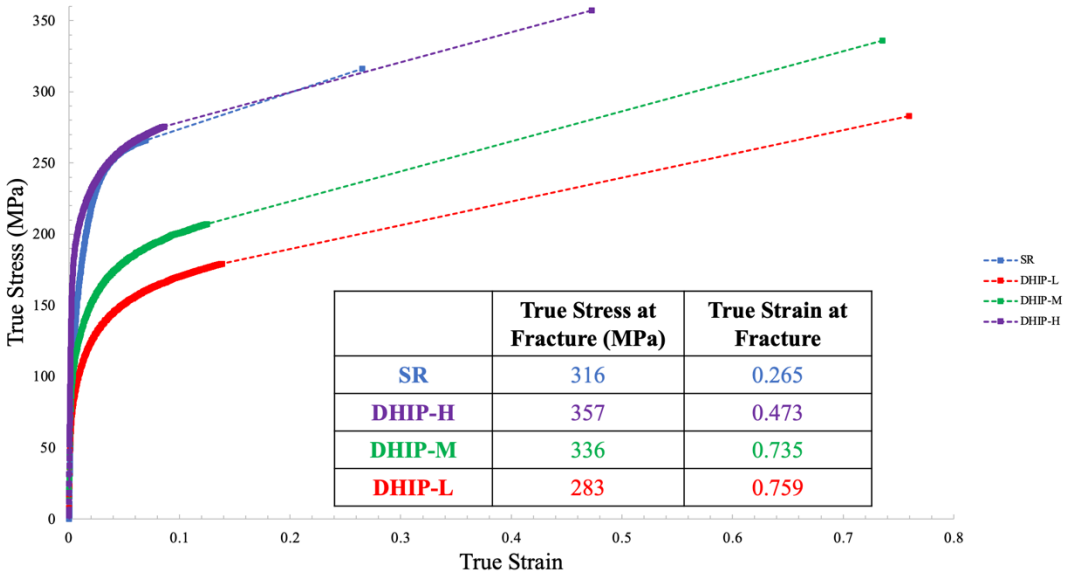

	True Stress at Fracture (MPa)	True Strain at Fracture
SR	316	0.265
DHIP-H	357	0.473
DHIP-M	336	0.735
DHIP-L	283	0.759

Figure 20: SR and DHIP conditions true stress-strain curves and their associated true stress and strain at fracture

and elongation, paired their standard deviations (n=3 for each condition). The engineering stress strain curves reveal that with increasing cooling rates, the strength is increased, but the ductility is decreased. The mean UTS for DHIP-H, DHIP-M, and DHIP-L are 254 MPa, 183 MPa, and 157 MPa respectively, while the mean engineering strains at fracture are 16.7%, 18.8%, and 22.3% respectively. The SR condition experienced a mean UTS of 244 MPa, and a mean engineering strain at fracture of 10.3%, which was outperformed by the DHIP-H condition, indicating that the DHIP-H condition can provide superior mechanical properties in comparison to the SR condition. Moreover, referring to figure 20, the true stress true - strain performance shows a substantial improvement in the true strain at

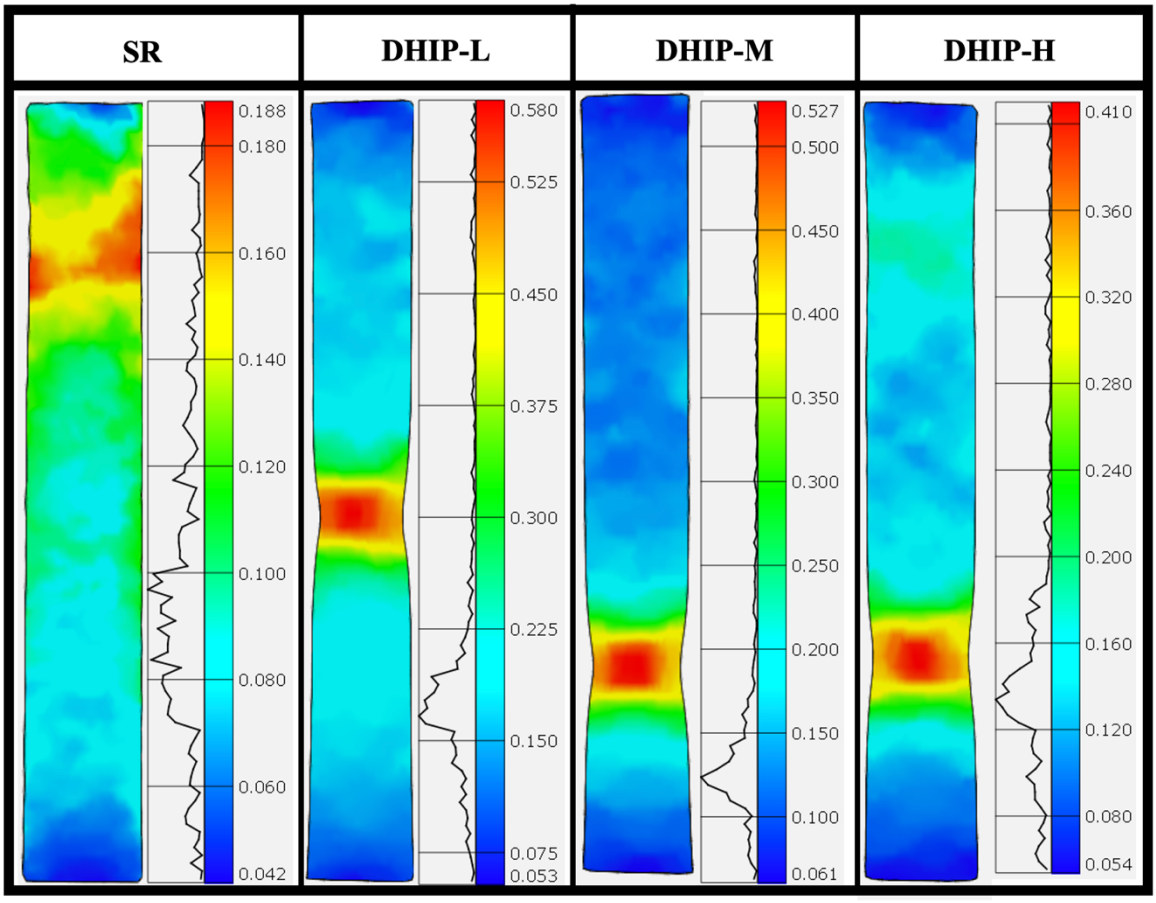

Figure 21: 2D DIC representative data for the SR condition and the DHIP conditions

fracture when comparing the SR condition to the DHIP-H condition. DHIP-H experienced a true stress at fracture and true strain at fracture of 357 MPa and 0.473 respectively, while the SR condition experienced a true stress at fracture and true strain at fracture of 316 MPa and 0.265 receptively. DHIP-M and DHIP-L experienced similar true strains at fracture of 0.735 and 0.759 respectively, but DHIP-L had a true stress at fracture of 283 MPa while DHIP-M had a true stress at fracture of 336 MPa. The necking behaviour is shown in figure 21. The 2D DIC data shows that the strain in DHIP samples has a peak in the histogram for low strain values, indicating that most of the sample surface experiences a low strain, except for the neck, therefore indicating a localized strain event occurring at the neck. The SR sample however does not have a distinct peak as with the DHIP specimens, therefore indicating that the strain values are more distributed and therefore, no severe localized necking occurs.

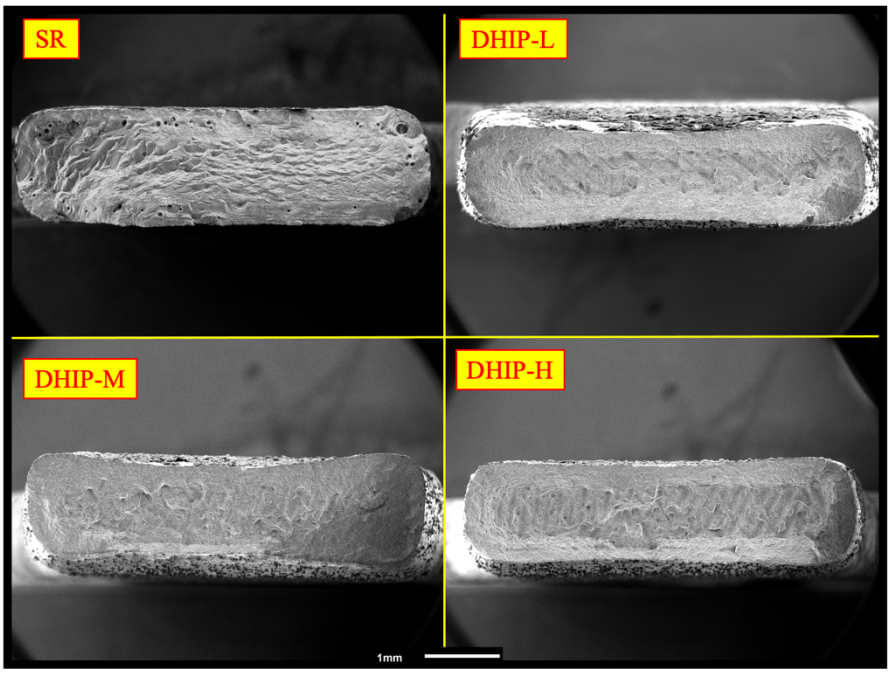

Figure 22: Fracture surfaces of DHIP and SR at x25 magnification

The fracture surfaces of the SR and DHIP conditions were studied using secondary electron imaging. The fracture surfaces were examined at various magnifications including x25, x2000, and x5000. The fracture surface images can be found in figure 22, figure 23, and figure 24 respectively. At low magnifications, it is evident that all DHIP specimens experienced localized necking (through a reduction in the cross-sectional area), and the perimeter of each DHIP samples shows evidence of shear lips. At the center of all DHIP specimens, evidence of laser tracks is observed. The SR sample, however, shows evidence of a crack initiating on the bottom left corner of the specimen. The SR specimen also features large scale voids along the perimeter of the fracture surface, which is not evident in the DHIP specimens due to the pressure experienced during its post-processing. At higher magnifications, there is evidence of dimples on all fracture surfaces, including the

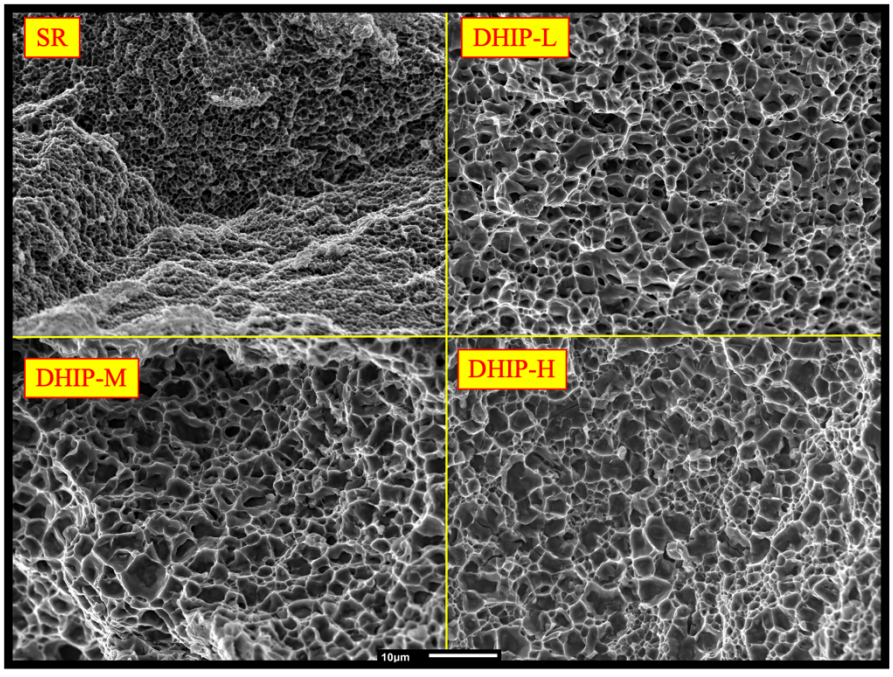

Figure 23: Fracture surfaces of DHIP and SR at x2000 magnification

SR condition. The dimples on all DHIP specimens however, are much larger than that of the SR condition.

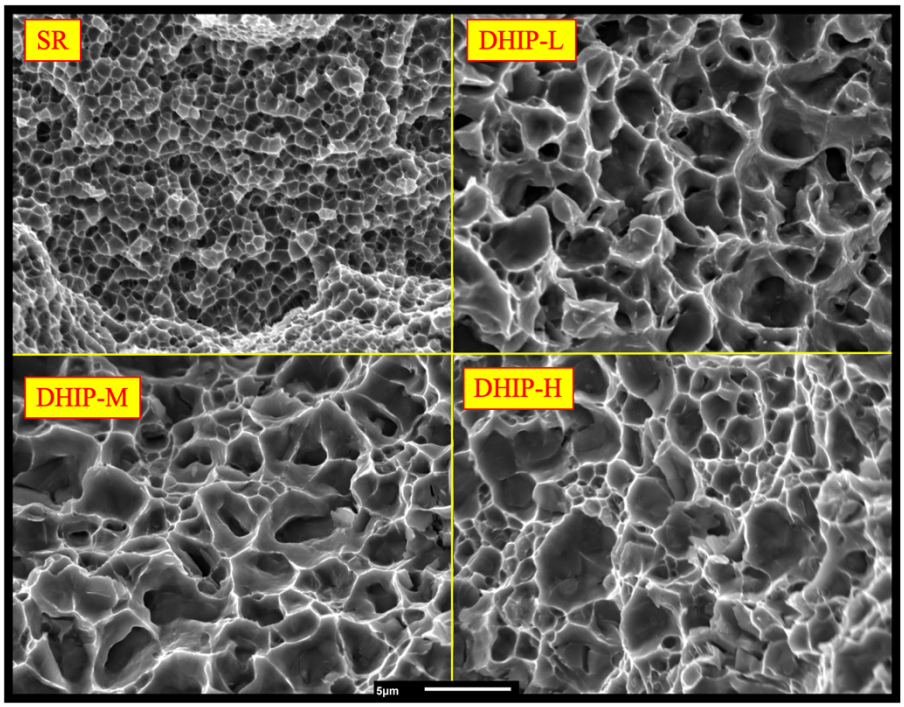

Figure 24: Fracture surfaces of DHIP and SR at x5000 magnification

5.4.0 DHIP and SR Microstructure

The microstructure of DHIP and SR was imaged through the use of secondary electron imaging at x10,000 magnification. Microstructurally, the same features exist

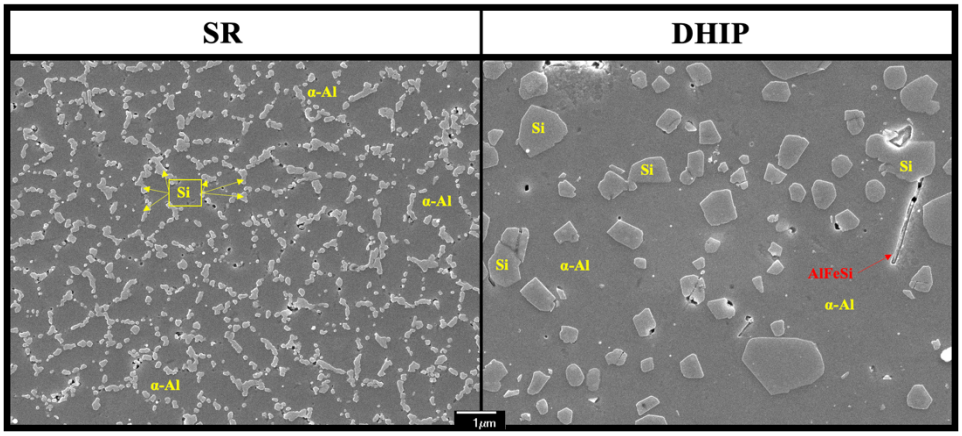

Figure 25: Microstructure images with their associated phases labelled for the SR and DHIP condition (DHIP-L is represented here)

within DHIP-L, DHIP-M, and DHIP-H, therefore, a representative microstructure was used (DHIP-L) and can be seen in figure 25. The SR condition features small Si precipitates that surround the α-Al grains. In the DHIP conditions, the Si precipitates are much larger in size, and are located within the α-Al matrix, along with a needle shaped intermetallic particle (AlFeSi).

5.4.1 In-situ Tensile Testing via SEM coupled with μ-DIC

This section will present the results of the in-situ tensile tests via SEM coupled with μ-DIC. These tests were conducted mainly at x2,500 and x5,000 magnification, however, a test was conducted at x30,000 specifically for the SR condition due to the nature of how fine the silicon particles are. For the DHIP conditions, x5,000 was adequate to observe the behavior of the Si particles. Results for the x2,500, x5,000, and x30,000 tests can be found in figure 26, figure 27 and figure 28 respectively. The microstructure for these tests had a speckle pattern applied to them through the use of colloidal silica, therefore, the images will be populated with fine colloidal silica particles, which will be different than what is seen in figure 25.

The average strain of the Si phase and the α-Al phase for each condition was calculated and plotted as a function of the local average true strain (in other words, the average of the whole 2D DIC map). This graph is shown in figure 9, superimposed with a line (slope=1) to represent what homogenous deformation would look like. For example, if a single-phase material were to deform, in theory it should have a slope of one, because the local average strain would be equivalent to the average phase strain. In the case of a material with two or more phases present, there is a partitioning of the strain that occurs; therefore, it is a good outline to have the slope=1 line present in the graph.

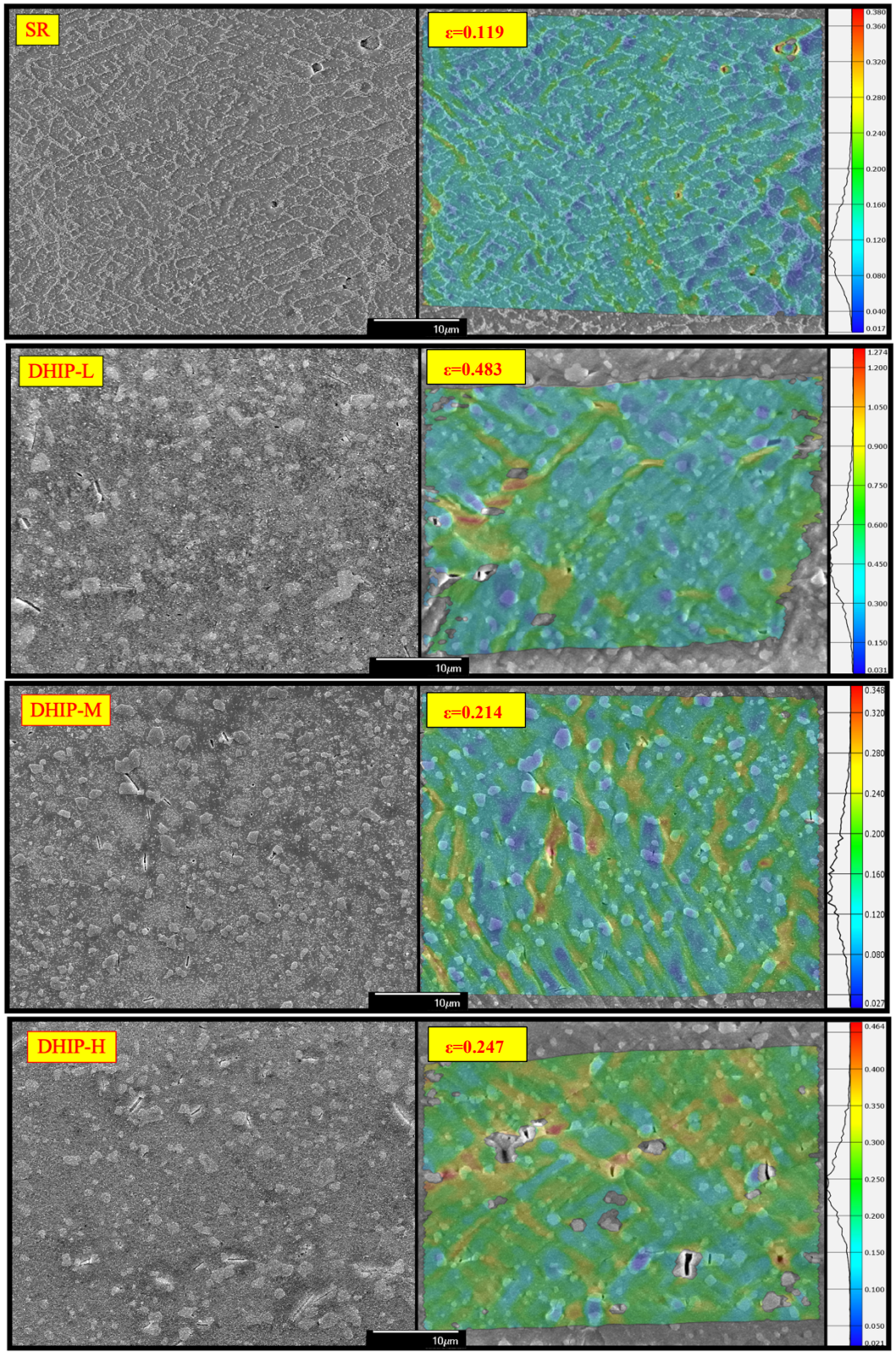

Figure 26: μ-DIC results for all DHIP conditions and the SR condition at x2,500 magnification (left column images represent the undeformed state)

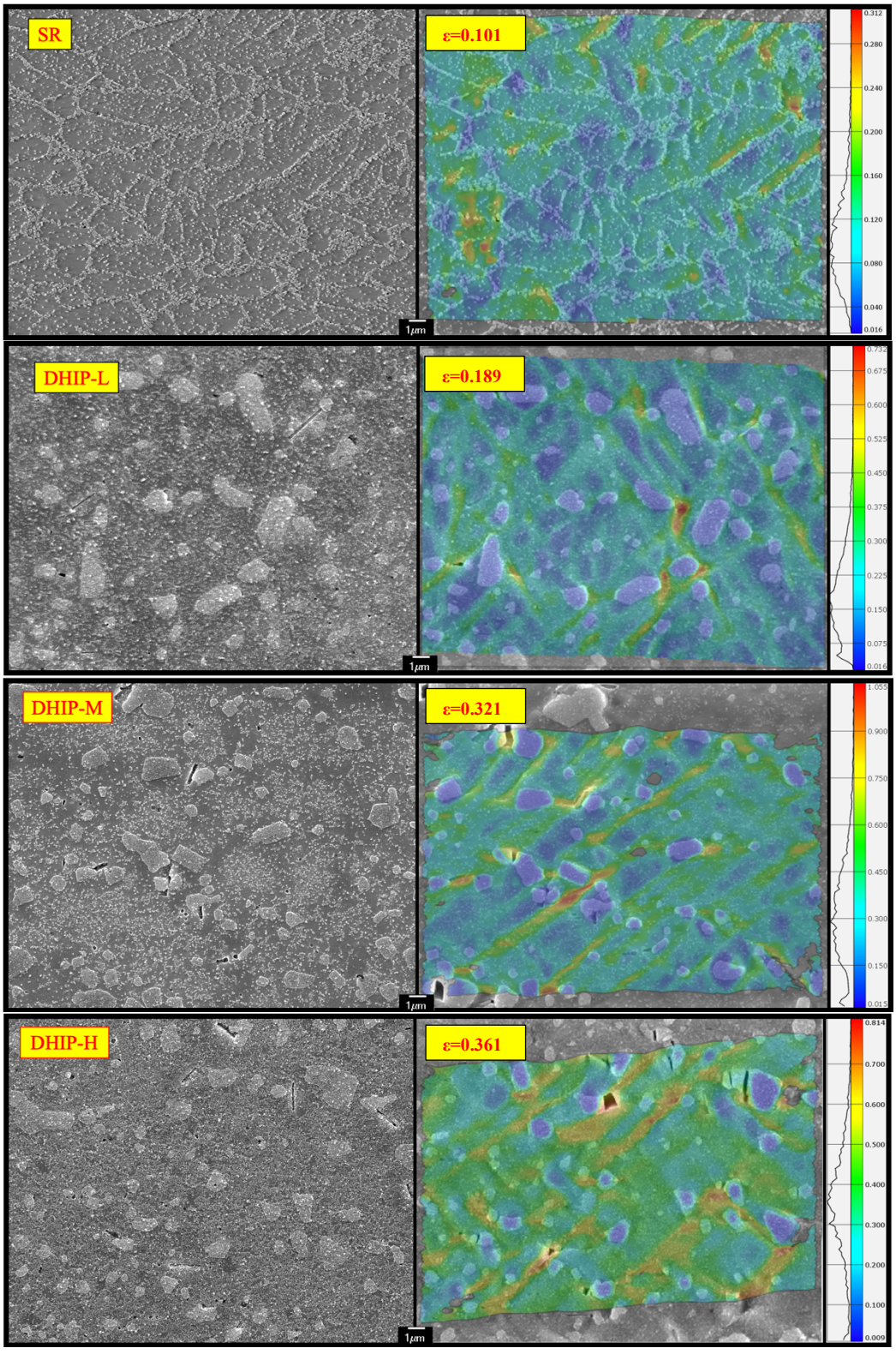

Figure 27: μ-DIC results for all DHIP conditions and the SR condition at x5,000 magnification (left column images represent the undeformed state)

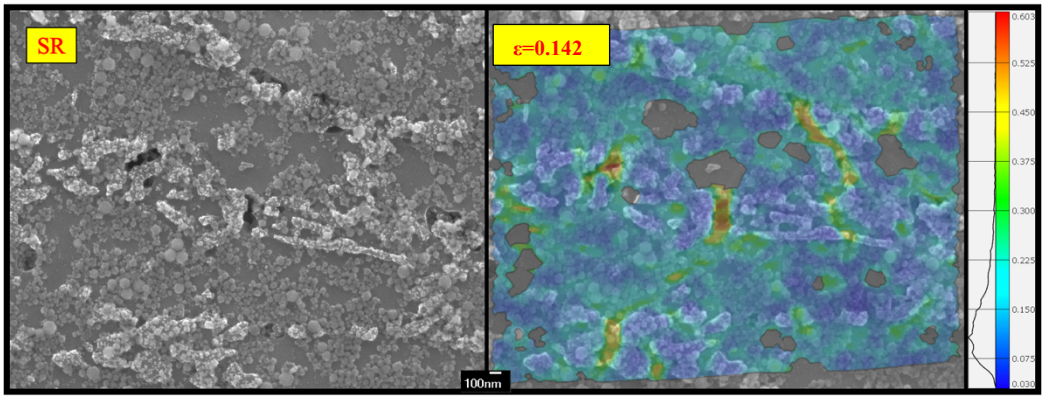

Figure 28: μ-DIC result for the SR condition at x30,000 magnification (left image represents the undeformed state)

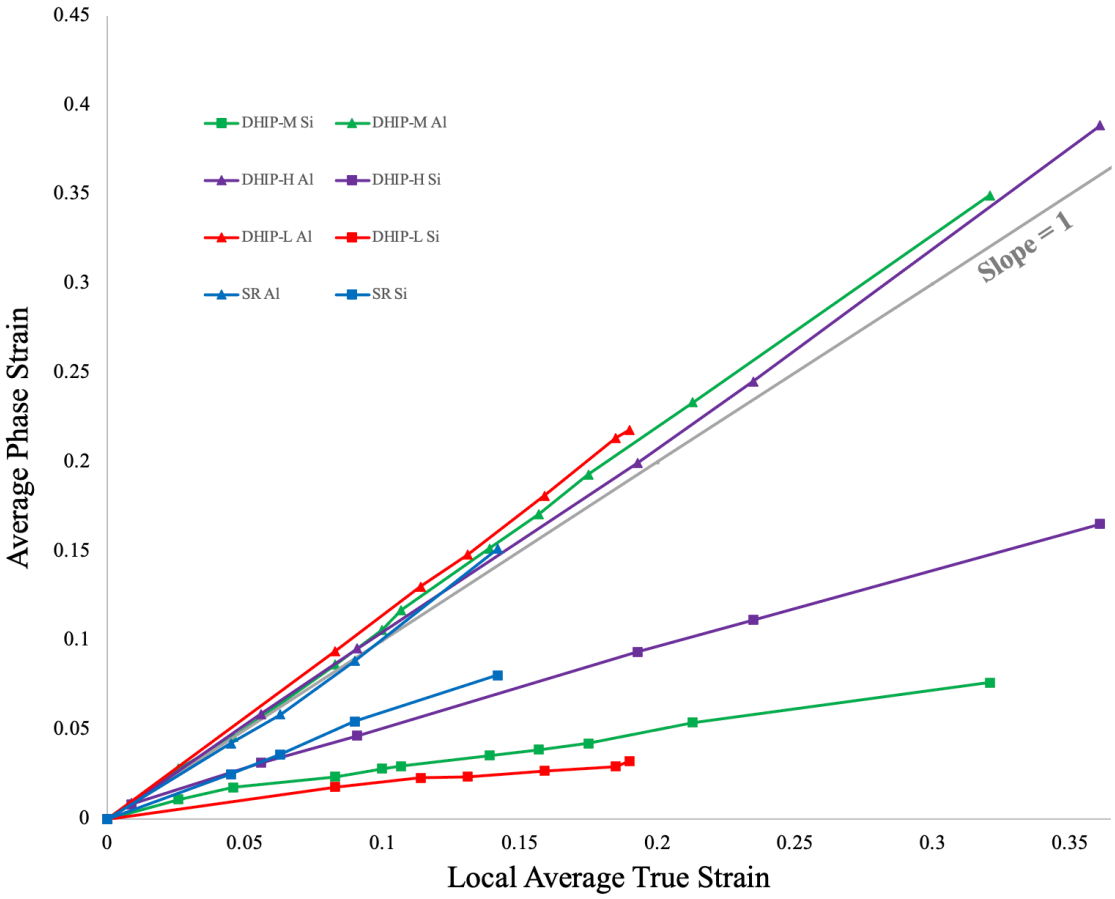

Figure 29: Average phase strain as a function of the local average true strain for all DHIP conditions and the SR condition. Triangular points represent the strain in the Al phase, and square points represent the strain in the Si phase.

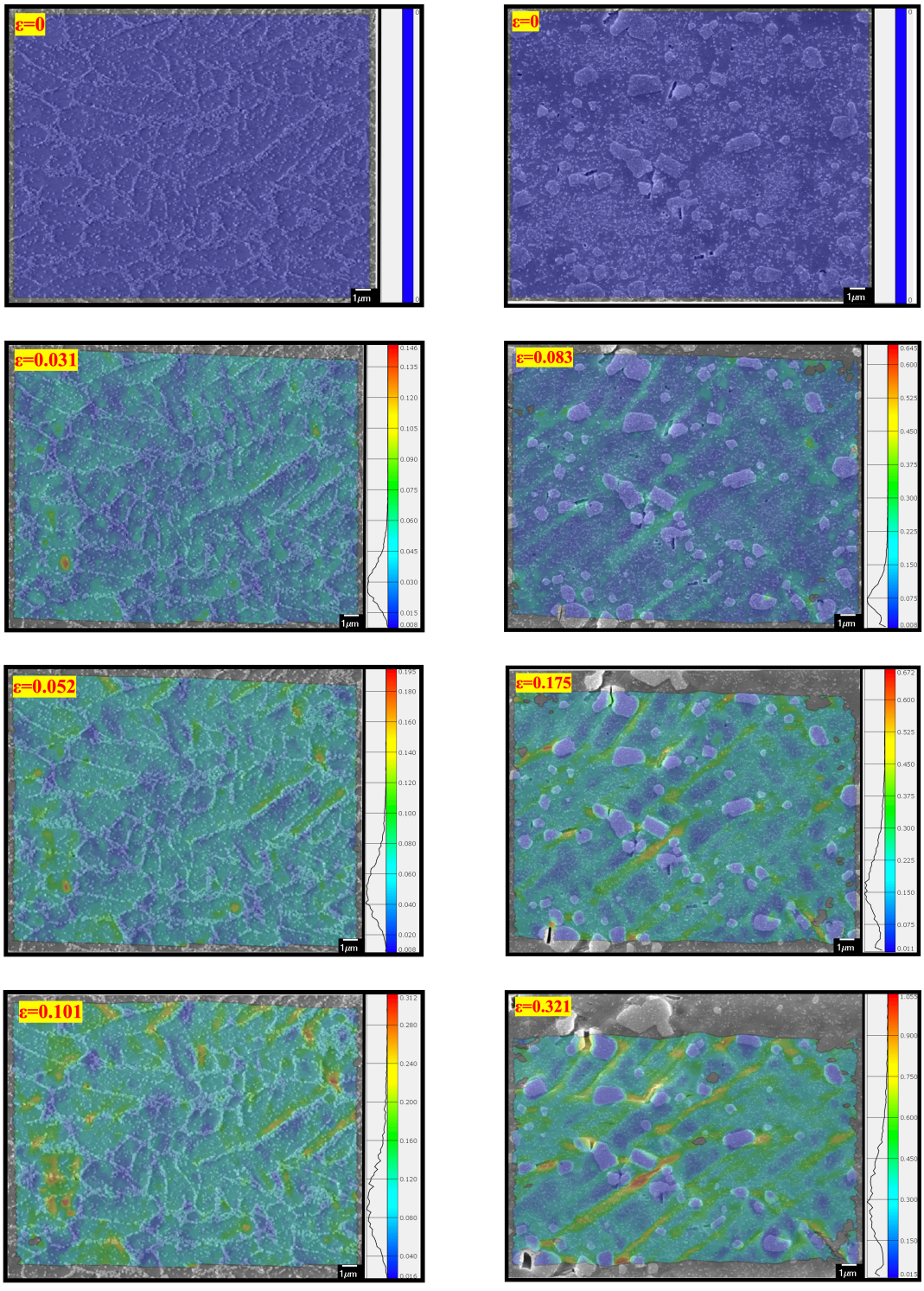

Figure 30: The progression of deformation as a function of local average true strain (indicated in the top left corner of each image). The left column represents the SR condition, and the right column represents the DHIP-M condition (both x5000 magnification).

Figure 30 shows the progression of deformation with DIC maps representing the local strain. The left column shows the SR condition at x5000 magnification, and the right column shows the DHIP-M condition at x5000 magnification. The SR condition shows consistent strain localization along the interface between the Si precipitates and the α-Al phase. The DHIP-M condition however shows strain to begin to localize in-between adjacent Si particles, and as the strain progresses, cracks start to form within Si particles, ultimately leading to particle fracture. This particle fracture behaviour has been observed in all DHIP conditions.

5.4.2 In-situ Tensile Testing via XCT

In this project, only the SR condition and the DHIP-M condition underwent in-situ tensile testing via XCT. The average void density was calculated every step in the interrupted tensile test and plotted against the true strain and is shown in figure 31. It was

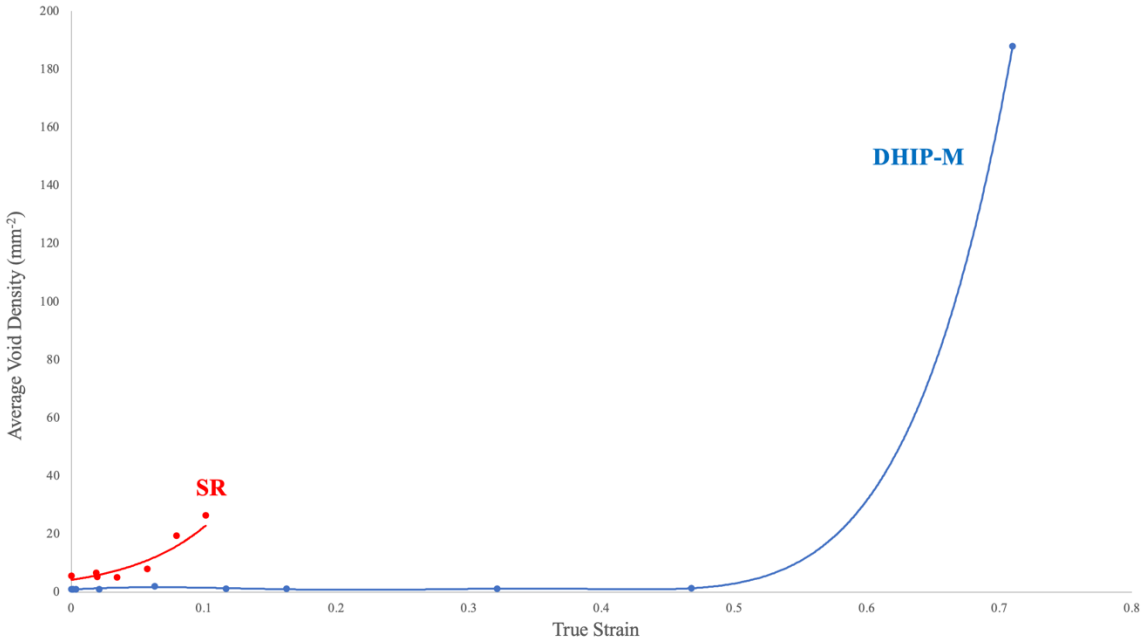

Figure 31: The average void density plotted against true strain for both DHIP-M and SR

observed that with the DHIP-M condition, the average void density does not increase at all, until just under a true strain of 0.5, where a huge increase is observed. The SR condition starts its deformation process with a higher average void density, and as strain is applied, a slow, an increase is observed. Using the scan of the fracture tip, it is also possible to calculate the void density per slice, and it can be plotted against the true strain. This is done by obtaining the void density data per slice, and by using the area in each slice, a true strain can be back calculated against the original area. This graph can be found in figure 32. This result agrees with figure 31, with regards to the increase of the void density at higher true strain values. The SR condition features regions of peaks and values with respect to the void density, which represents pre-present porosity in the material. Similarly, on a slice-by-slice basis of the fracture tip, the void area fraction was calculated as a function of true

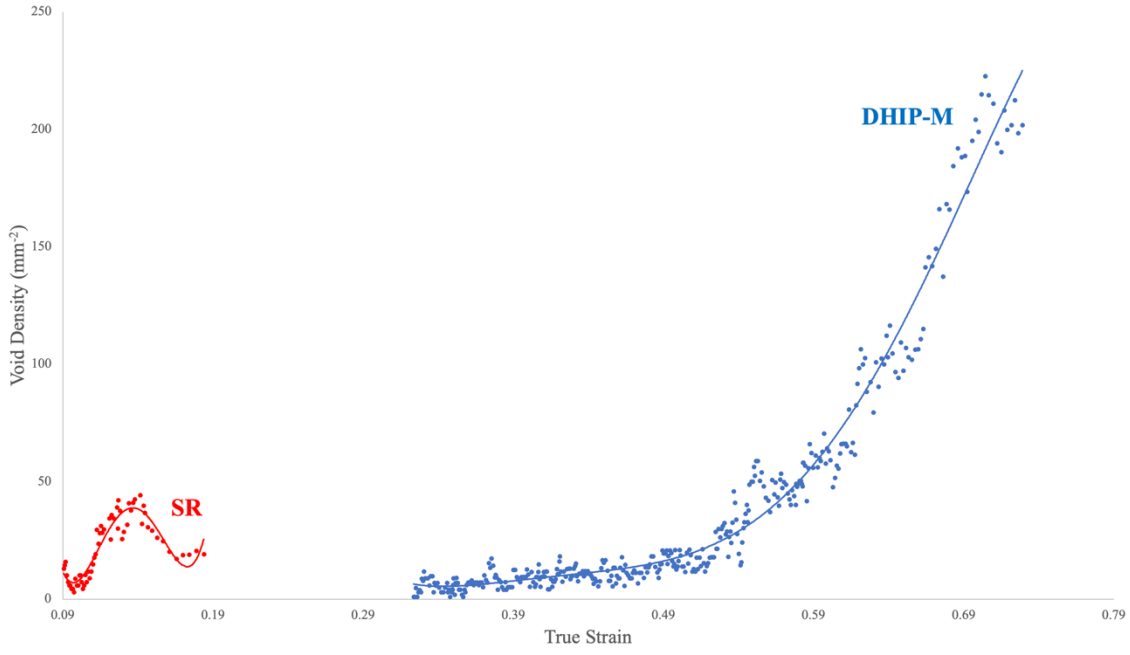

Figure 32: The void density per slice plotted against the true strain for the DHIP-M condition and the SR condition

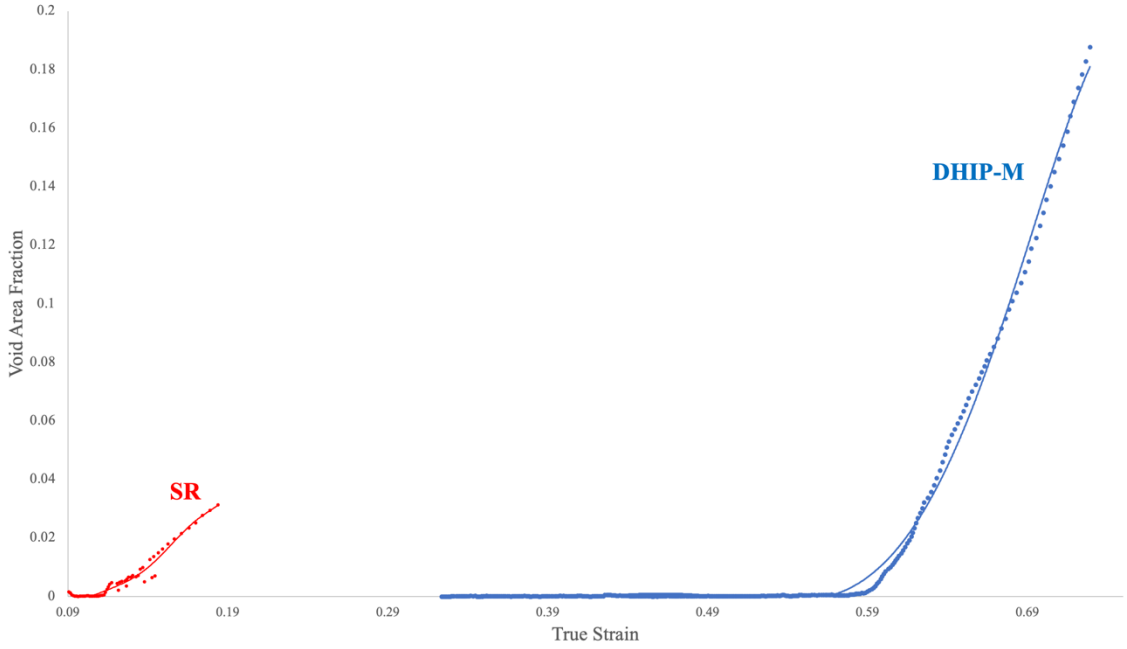

Figure 33: The void area fraction per slice plotted against the true strain for the DHIP-M condition and the SR condition

strain and can be found in figure 33. This result indicates that there is a much higher void area fraction with the DHIP-M condition near the tip of the fractured specimen over the SR condition. The same peaks and valleys can be observed at low true strain values for the SR condition, which are attributed to the pre-present porosity. Lastly, figure 34 presents the average void area fraction with respect to the true strain. On average, at low strains the SR condition experiences a higher average void area fraction, and as the specimens approaches fracture, the average. Increases. The DHIP-M condition has averages very closer to 0 at true strains before fracture but experiences a large value of the void area fraction at a high true strain value.

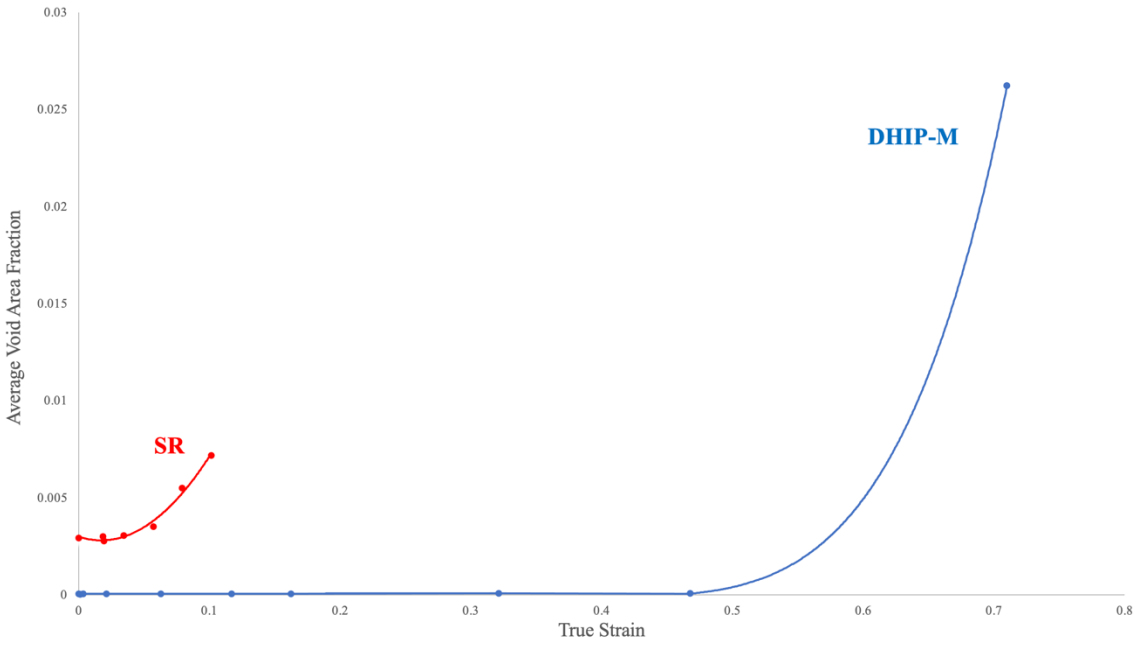

Figure 34: Average void area fraction plotted against the true strain

6.0.0 Discussion

6.1.0 Heat Treatment Study

The purpose of this study was to ensure adequate homogenization of the microstructure, in the least time possible. It was observed (see figure 14) that all homogenization times (30 minutes, 60 minutes, and 120 minutes) provided an adequate level of homogenization. This is in line with what is seen through Takata's microstructural investigations, as shown in figure 5 [12].

Microhardness results indicated that there is no significant difference in the Vickers hardness properties between the three homogenization times in the artificially aged state and non-artificially aged state. This is visually and numerically shown in figure 15 and table 5. However, although the hardness results were consistent regardless of the homogenization time, uniaxial tensile testing showed that the properties differ. The samples that experienced 30 minutes of homogenization experienced a higher strength and a decreased ductility when comparing to the samples that experienced a homogenization of 120 minutes (for both aged and non-aged conditions). This is indicative of microstructural coarsening occurring with increased homogenization time (refer to figure 16).

6.1.1 Quench Sensitivity Analysis

In reference to table 6 and figure 16, it was observed that the change in Vickers hardness from the T4 to T6 condition increases, with increasing quench rate. The hardness increases with increased quench rate, but the strongest effect occurs up to 15K/s, after which there is a slow increase between the 15K/s (18.17 HV) and 200K/s (19.6 HV).

6.2.0 Mechanical Properties Orientation Effect

In reference to figure 17, the as-built properties show a clear mechanical property heterogeneity with respect to the orientation the specimen is built in. This phenomenon was observed by Salib et al. [24], whereby an observation of a mechanical property heterogeneity was present through hardness testing across the build direction. The hardness results showed that layers closest to the build plate featured low hardness values in comparison to layers furthest away from the build plate, which featured a higher hardness value. Comparing this result to figure 17, the horizontal specimen had the least strength. This is due to most of the specimen experiencing heat from the build plate, therefore softening most of the material, while the vertically built specimens did not experience as much heat from the build plate (relatively).

After the stress relieving treatment, the mechanical properties were homogenized in contrast to the as-built condition. The homogenized mechanical properties could be attributed to the stress relieving treatment eliminating the hardening achieved along meltpool boundaries due to the high cooling rates from the SLM process [13].

6.3.0 Effect of Cooling Rate During Direct HIP
6.3.1 Mechanical Properties of DHIP

It is evident that there is a large difference in mechanical properties when comparing different cooling rates after solution annealing. There are two main factors to consider when discussing the effect of cooling rate on the mechanical properties of AlSi10Mg after solution annealing. The first is precipitation hardening, which is substantially different when considering cooling rate. At high cooling rates (e.g. DHIP-H), it is expected that finer precipitates are formed with a uniform distribution, which is expected to increase the

strength of the material due to the increased number of uniformly distributed particles that impede dislocation movement. This is due to the nature of high cooling rates which tend to trap more solute atoms in the solid solution. On the other hand, at lower cooling rates (e.g. DHIP-L), larger precipitates with wider precipitate spacing is to be expected, which results in a reduction in strength due to the decrease in precipitates that are able to impede on dislocation movement. The second factor is Ostwald ripening. At high cooling rates, Ostwald ripening is suppressed, therefore finer particles are formed relatively to lower cooling rates, which relatively experience a higher degree of coarsening (or Ostwald ripening). This explains why there is a large difference in mechanical properties between DHIP-H, DHIP-M, and DHIP-L.

The macro-scale fracture surfaces are shown in figure 22. The SR condition shows evidence of a crack initiating from the bottom left corner of the specimen, and then

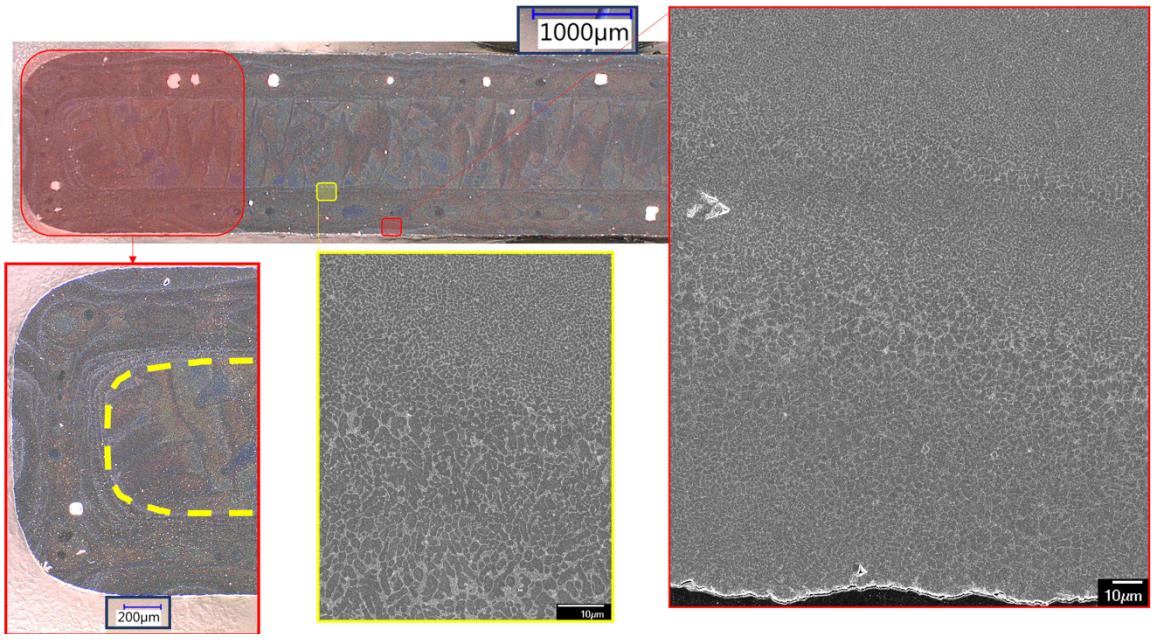

Figure 35: Cross section of a vertically built specimen (tensile direction is in and out of the page)

propagating inwards, therefore causing fracture. There is also evidence of pores along the perimeter of the SR condition. DHIP-H, DHIP-M, and DHIP-L all show evidence of shear lips on the perimeter of the fracture surfaces, with evidence of decoherence of meltpool boundaries at the core. The shear lips could be associated with a microstructural heterogeneity associated with the SLM process. To improve the surface finish of the SLM component, when a layer is completed, the laser will pass around the perimeter of the layer using a higher laser power to smooth the surface finish. A series of microscopy images visually depict this in figure 35. Observing the fracture surfaces at x2,000 and x5,000 (figure 23 and 24 respectively) shows that all surfaces feature dimples on the surface, indicative of void growth and coalesence. The dimples on the SR surface appear to be much finer than that of the DHIP specimens, due to the microstructural corasening the DHIP specimens experience.

6.3.2 Comparison of Mechanical Properties to Literature

Although there is no work in literature that utilizes a direct HIP approach as in this project, a comparison of DHIP-H can be made to the SR conditions studied in literature. This is an effective comparison because the goal of this work is to outperform the SR condition, because it is the only post-processing method of interest that doesn't utilize water quenching. Ertugrul et al. [15] reported that after annealing at 300°C for 2 hours (which is the same treatment as the SR condition presented in this project), the yield strength was 210 ± 16 MPa, with a UTS of 302 ± 15 MPa, and a strain to failure of 10.7 ± 1.6%. Comparing to the SR data from this project, which had a yield of 149 ± 3 MPa, UTS of 244 ± 4 MPa, and a strain to failure of 10.3 ± 0.8%, there is a clear difference in mechanical

properties that do not agree with each other. This could be attributed to a difference in printing parameters used, or it could be attributed to the fact that cylindrical specimens were used in Ertugrul's work. When comparing with DHIP-H, which had a yield of 197 ± 1 MPa, UTS of 254 ± 2 MPa, and an elongation of 16.7 ± 0.4 %, it is clear that the DHIP-H condition exhibits a lower strength, but superior ductility to Ertugrul's SR condition. However, Finfrock et al [16] reported an SR behavior that did not perform as well as the SR condition presented in this project. Finfrock's SR condition also featured 300°C for 2 hours, but the reported mechanical properties showed a UTS of about 170 MPa and a strain of about 7% (the yield strength was not presented). These results show a substantial decrease from 244 MPa as reported in this project. This makes a strong case that the mechanical properties of AlSi10Mg manufactured through SLM strongly depend on the printing parameters.

The novel DHIP approach aims to be a strong competitor against popular cast aluminum alloys, such as AA6061-T6 and A359. The ASTM handbook reports that AA6061-T6 has a yield strength of 275 MPa, UTS of 275 MPa, and an elongation of 12%. Radhakrishan et al. [18] reported a yield strength of 276 MPa, UTS of 328 MPa, and an elongation of 12%. Both sources outperform DHIP-H with respect to strength, however, DHIP-H outperforms both reports of AA6061-T6 when it comes to ductility, with an increase of about 4%. With respect to A359 that underwent T6, the ASTM handbook reported having a yield strength of 290 MPa, UTS of 345 MPa, and an elongation of 5.5%. Similarly, to AA6061-T6, from a strength perspective, DHIP-H is less superior, but with respect to elongation, DHIP-H strongly outperforms A359. In general, when comparing to

AA6061 and A359, it is evident that DHIP-H has superior ductility properties but lacks in strength.

6.3.3 In-situ Tensile Testing via SEM coupled with μ-DIC

The tests that were conducted at x2500 magnification revealed that for all DHIP conditions, shear bands are present in the deformation process, while in the SR condition, shear bands were not observed. Evidence of strain localization around a defect can be seen in the top right corner of the SR condition. At x5,000 magnification, the SR condition features strain localization along the interface between the α-Al phase and the Si phase, while in the DHIP conditions, the strain localizes and flows in-between two adjacent Si particles. Furthermore, the DHIP conditions experience Si particle fracture, but it is not as prevalent in the DHIP-L condition. This could be due to the fact that the location in which that test was conducted was not as close to the fracture tip, as the other specimens, indicating that there is still a possibility for those particles to fracture at higher strains. The calculation of the average phase strain as a function of average local strain can shed light on this issue as well. In reference to figure 29, it is observed that in DHIP-L, the strain experienced in the α-Al is higher than DHIP-H and DHIP-M, while the strain experienced by the Si phase is the lowest. This can be attributed to the idea that at high cooling rates, fine precipitates are nucleated in a uniform manner in the α-Al matrix, therefore introducing a higher strength in the matrix over the lower cooling rates, and therefore the α-Al matrix at low cooling rates will experience a higher strain. Although in theory, DHIP-L should have the highest local average true strain as the last point in the graph, however, the region in which the images were taken were not as close to the fracture tip as compared to DHIP-

M and DHIP-H. At x30,000, the SR condition showed that strain also flows between two adjacent Si particles, and according to the data seen in figure 29, the SR condition features the highest strain experienced by the Si phase. This is the case because the SR condition experienced the highest cooling rate after the SLM process [3].

6.3.4 In-situ Tensile Testing via XCT

In reference to figure 31, the average void density is shown as a function of true strain. The void density refers to the void count within the specimen. As such, it is an indication of void nucleation if it increases as a function of true strain. It is seen that the average void density for the DHIP-M specimen is very low in the early stages of deformation, but as it nears fracture, the void density increases at a high rate. With regards to the SR specimen, the average void density values in the early stages of deformation are relatively higher than the DHIP-M specimen, due to the presence of pre-present pores (since the SR specimen did not experience pressure during its post-processing). As the SR specimen nears fracture, the increase is not as substantial as the DHIP-M specimen, therefore indicating that DHIP-M gives rise to more voids being nucleated. This is a clear indication that the DHIP-M condition is far more damage tolerant than the SR condition. It is important to note the voxel size is approximately 1.05 μm^3, which means, to adequately characterize a void or pore, the void or pore cannot be smaller than 1.05 μm^3. Therefore, features that are greater 1.05 μm^3 are recognizable by the XCT. Referring to figure 24, the x5,000 fractography data shows that the dimples on the SR specimen are extremely small, on the order of 0.5-2 μm. Therefore, it is important to note that there could be some missing information as a limitation of the resolution of this test. Figure 32 shows the void density

as a function of true strain, except on a slice-by-slice basis, and it shows to be in agreement with figure 30 with respect to trend and quantities.

Void area fraction describes the area of voids divided by the area of a slice in the material, therefore, representing the fraction of voids in 2D, per slice. This metric is an excellent way to gauge for growth of voids/pores in a material. Figure 33 shows the void area fraction as a function of the true strain on a slice-by-slice basis. The DHIP-M condition starts to see a substantial increase in the void area fraction at a true strain value of approximately 0.6, while the SR condition experiences fluctuations in the void area fraction throughout, due to the pre-present pores, and features a slight increase at a true strain value of approximately 0.1. The average void area fraction data (figure 34) shows a similar trend to its counterpart in figure 32, however, the average void density curve for the SR condition

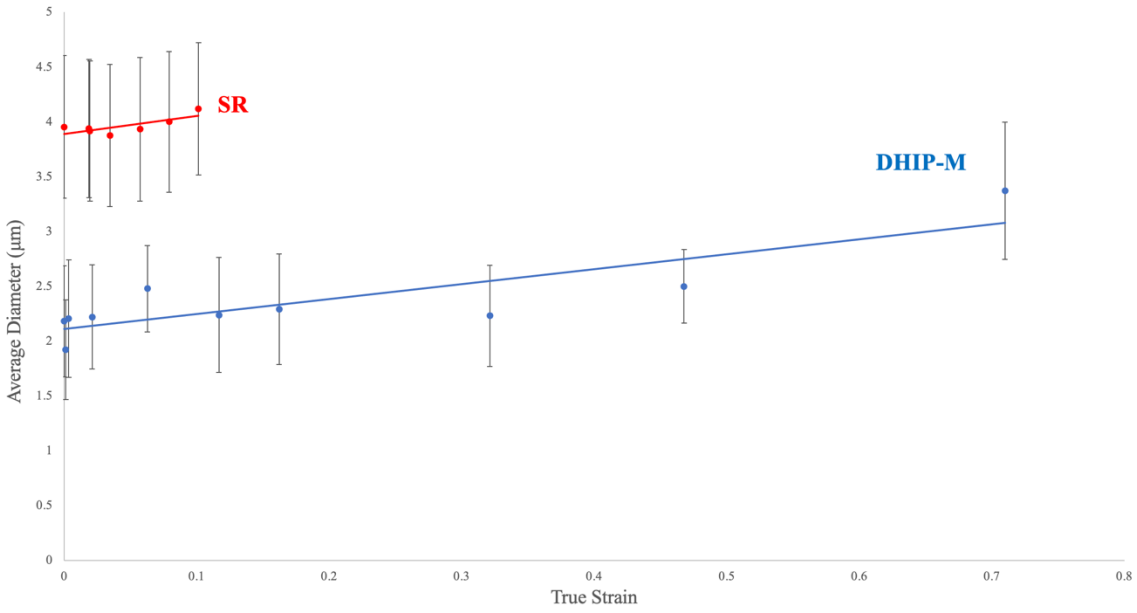

Figure 36: The top 50 voids average diameter as a function of the true strain

shows high values at low strains. This is indicative the pre-present porosity dominating the average value, therefore raising the curve above the DHIP-M condition.

The data from the void density calculations and the void area fraction calculations confirm the true strain behaviour seen in figure 20, whereby the observed true strain for the SR condition was 0.265, and 0.735 for the DHIP-M condition. In the in-situ tensile tests via XCT, it was seen that the SR condition reaches a true strain of about 0.11, while the DHIP-M condition reached a value of about 0.71. The values for the DHIP-M condition are close, however, for the SR condition, there is a substantial difference. This can be attributed to the idea that failure is mainly driven through crack initiation in the SR condition. This was observed in figure in figure 22 on the macro scale. A 3D model of the SR specimen in the XCT revealed that a crack formed through a pre-present pore on the surface of the specimen, therefore leading to early fracture in the material (see figure 37). This is hypothesized to be the reasoning for the lower strain value in this experiment.

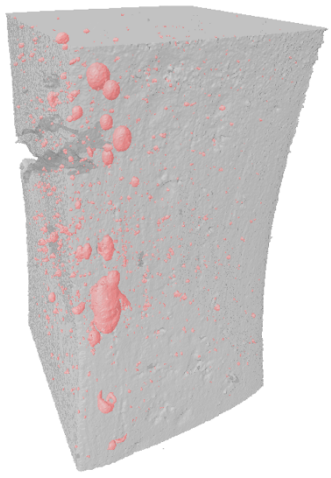

Figure 37: 3D model before fracture of the SR specimen indicating crack formation mid-deformation

To study the effect of pre-present porosity in the material, tracking the top 50 largest voids in the material is a great way to do so. In reference to figure 36, it is shown that the average diameter of the SR condition stays consistent with increasing true strain, while the DHIP-M specimen increases a slight increase as a function of true strain.

7.0.0 Conclusions

A novel approach using HIP to achieve a higher strength and ductility than the stress relieved condition without the use of water quenching was successfully tested using uniaxial tensile testing coupled with 2D DIC, in-situ tensile testing via SEM coupled with μ-DIC, and in-situ tensile testing via XCT. The key conclusions are as follows:

- The use of DHIP-H was able to successfully provide a higher strength and ductility than the SR condition, without the use of water quenching to reduce the severity of part distortion
- Popular aluminum alloys such as AA6061-T6 and A359 still have a superior strength than DHIP-H, however, DHIP-H produces a superior ductility
- Microstructurally, the SR condition experiences strain localization along the interface of the Si particles and the α-Al phase, while the DHIP conditions feature damage due to particle fracture
- At lower cooling rates, microstructurally, more strain is found in the α-Al phase, and less strain is found in the Si particles
- The XCT data revealed that DHIP-M experiences more void growth and nucleation right before fracture than the SR condition, indicating that DHIP-M is more damage tolerant

8.0.0 Future Work

DHIP-L and DHIP-H will also undergo in-situ tensile testing via XCT for a full comparative analysis. It is also recommended that the SR condition test is redone in a XCT apparatus capable of smaller voxel size due to the fracture surface revealing dimple sizes ranging between 0.5-2 µm. Furthermore, after the in-situ tensile tests via SEM, the fracture tip revealed evidence of microstructural damage along the meltpool boundary (see figure 38). It is recommended that a µ-DIC study takes place at approximately x1000 magnification in order to study the effect of the meltpool boundary for all conditions.

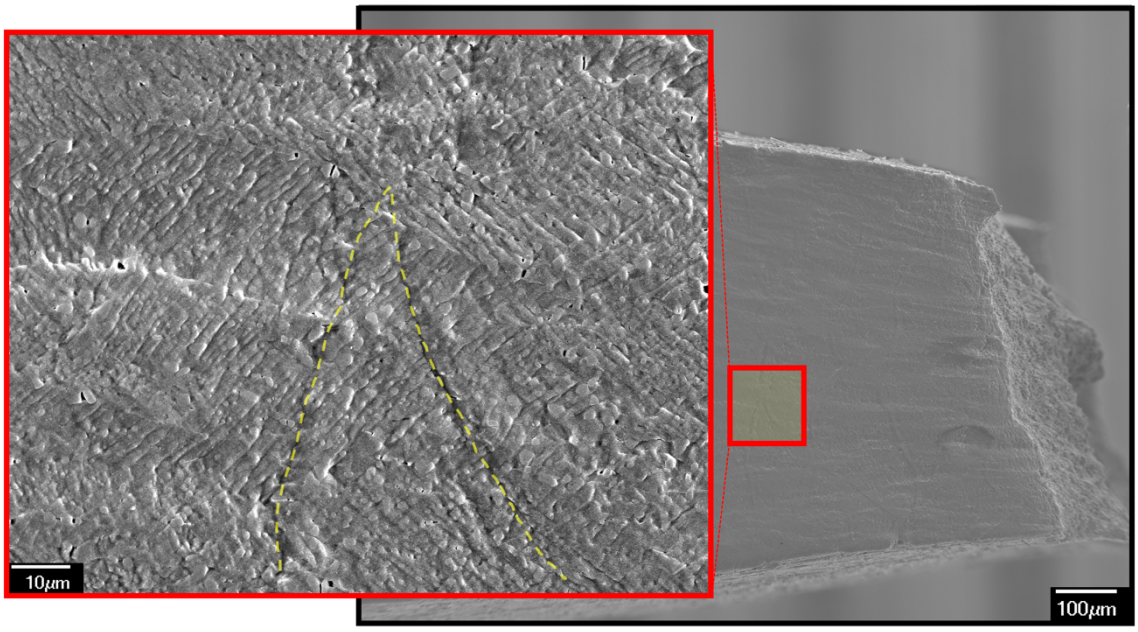

Figure 38: Evidence of damage along the melt pool boundary in DHIP-L (left image x1000, right image x95)

9.0.0 References

[1] N. Limbasiya, A. Jain, H. Soni, V. Wankhede, G. Krolczyk, and P. Sahlot, "A comprehensive review on the effect of process parameters and post-process treatments on microstructure and mechanical properties of selective laser melting of AlSi10Mg," *J. Mater. Res. Technol.*, vol. 21, pp. 1141–1176, 2022.

[2] E. M. Sefene, "State-of-the-art of selective laser melting process: A comprehensive review," *J. Manuf. Syst.*, vol. 63, no. April, pp. 250–274, 2022.

[3] D. D. Ben *et al.*, "Heterogeneous microstructure and voids dependence of tensile deformation in a selective laser melted AlSi10Mg alloy," *Mater. Sci. Eng. A*, vol. 798, no. August, 2020.

[4] Z. H. Xiong, S. L. Liu, S. F. Li, Y. Shi, Y. F. Yang, and R. D. K. Misra, "Role of melt pool boundary condition in determining the mechanical properties of selective laser melting AlSi10Mg alloy," *Mater. Sci. Eng. A*, vol. 741, no. April 2018, pp. 148–156, 2019.

[5] N. T. Aboulkhair, M. Simonelli, L. Parry, I. Ashcroft, C. Tuck, and R. Hague, "3D printing of Aluminium alloys : Additive Manufacturing of Aluminium alloys using selective laser melting," *Prog. Mater. Sci.*, vol. 106, no. May, 2019.

[6] H. Shipley *et al.*, "Optimisation of process parameters to address fundamental challenges during selective laser melting of Ti-6Al-4V : A review," *Int. J. Mach. Tools Manuf.*, vol. 128, no. September 2017, pp. 1–20, 2018.

[7] J. Praneeth, S. Venkatesh, and L. S. Krishn, "Process parameters influence on mechanical properties of AlSi10Mg by SLM," *Mater. Today Proc.*, no. xxxx,

2023.

[8] Y. Wang and J. Shi, "Effect of hot isostatic pressing on nanoparticles reinforced AlSi10Mg produced by selective laser melting," *Mater. Sci. Eng. A*, vol. 788, no. March, p. 139570, 2020.

[9] L. Zhao, J. Guillermo, S. Macías, T. Douillard, and Z. Li, "Unveiling damage sites and fracture path in laser powder bed fusion AlSi10Mg : Comparison between horizontal and vertical loading directions," *Mater. Sci. Eng. A*, vol. 807, no. February, 2021.

[10] S. I. Shakil, A. Hadadzadeh, B. S. Amirkhiz, H. Pirgazi, and M. Mohammadi, "Additive manufactured versus cast AlSi10Mg alloy : Microstructure and micromechanics," *Results Mater.*, vol. 10, no. March, 2021.

[11] F. Alghamdi and M. Haghshenas, "Microstructural and small - scale characterization of additive manufactured AlSi10Mg alloy," *SN Appl. Sci.*, vol. 1, no. 3, pp. 1–10, 2019.

[12] N. Takata, H. Kodaira, K. Sekizawa, A. Suzuki, and M. Kobashi, "Change in microstructure of selectively laser melted AlSi10Mg alloy with heat treatments," *Mater. Sci. Eng. A*, vol. 704, no. May, pp. 218–228, 2017.

[13] I. Roveda, I. Serrano-Munoz, A. Kromm, and M. Madia, "Investigation of residual stresses and microstructure effects on the fatigue behaviour of a L-PBF AlSi10Mg alloy," *Procedia Struct. Integr.*, vol. 38, no. C, pp. 564–571, 2021.

[14] M. H. Abdelaziz, E. M. Elgallad, H. W. Doty, and F. H. Samuel, "Strengthening precipitates and mechanical performance of Al–Si–Cu–Mg cast alloys containing

transition elements," *Mater. Sci. Eng. A*, vol. 820, no. July 2020, p. 141497, 2021.

[15] O. Ertuğrul *et al.*, "Effect of HIP process and subsequent heat treatment on microstructure and mechanical properties of direct metal laser sintered AlSi10Mg alloy," *Rapid Prototyp. J.*, vol. 26, no. 8, pp. 1421–1434, 2020.

[16] C. B. Finfrock, A. Exil, J. D. Carroll, and L. Deibler, "Effect of Hot Isostatic Pressing and Powder Feedstock on Porosity, Microstructure, and Mechanical Properties of Selective Laser Melted AlSi10Mg," *Metallogr. Microstruct. Anal.*, vol. 7, no. 4, pp. 443–456, 2018.

[17] J. Hatch, "Aluminum: Properties and Physical Metallurgy," *ASM Int.*, pp. 351–378, 1984.

[18] K. Radhakrishnan, P. Parameswaran, A. G. Antony, and K. Rajaguru, "Optimization of mechanical properties on GMAW process framework using AA6061-T6," *Mater. Today Proc.*, vol. 37, no. Part 2, pp. 2924–2929, 2020.

[19] V. Pickerd, "Optimisation and Validation of the ARAMIS Digital Image Correlation System for use in Large-scale High-strain-rate Events.," pp. 1–32, 2013.

[20] J. Samei, L. Zhou, J. Kang, and D. S. Wilkinson, "Microstructural analysis of ductility and fracture in fine-grained and ultra fine-grained vanadium-added DP1300 steels," *Int. J. Plast.*, no. June 2017, pp. 0–1, 2018.

[21] C. Pelligra, J. Samei, J. Kang, and D. S. Wilkinson, "The effect of vanadium on microstrain partitioning and localized damage during deformation of unnotched and notched DP1300 steels," *Int. J. Plast.*, vol. 158, no. February, p. 103435, 2022.

[22] H. Chen, S. Patel, M. Vlasea, and Y. Zou, "Enhanced tensile ductility of an additively manufactured AlSi10Mg alloy by reducing the density of melt pool boundaries," *Scr. Mater.*, vol. 221, no. August, p. 114954, 2022.

[23] J. Samei, M. Amirmaleki, M. Shirinzadeh Dastgiri, C. Marinelli, and D. E. Green, "In-situ X-ray tomography analysis of the evolution of pores during deformation of AlSi10Mg fabricated by selective laser melting," *Mater. Lett.*, vol. 255, p. 126512, 2019.

[24] Y. Salib, "Investigating the Evolution of Damage in Additively Manufactured AlSi10Mg," Undergraduate thesis, McMaster University, 2021.

[25] EOS GmbH, "EOS Aluminium AlSi10Mg Material Data Sheet," 2022.

[26] ASTM International, "Standard Test Methods for Tension Testing of Metallic Materials," vol. 3.01.

10.0.0 Appendix

A.1 ASTM E8 Subsize Flat Tensile Coupon (units: mm)

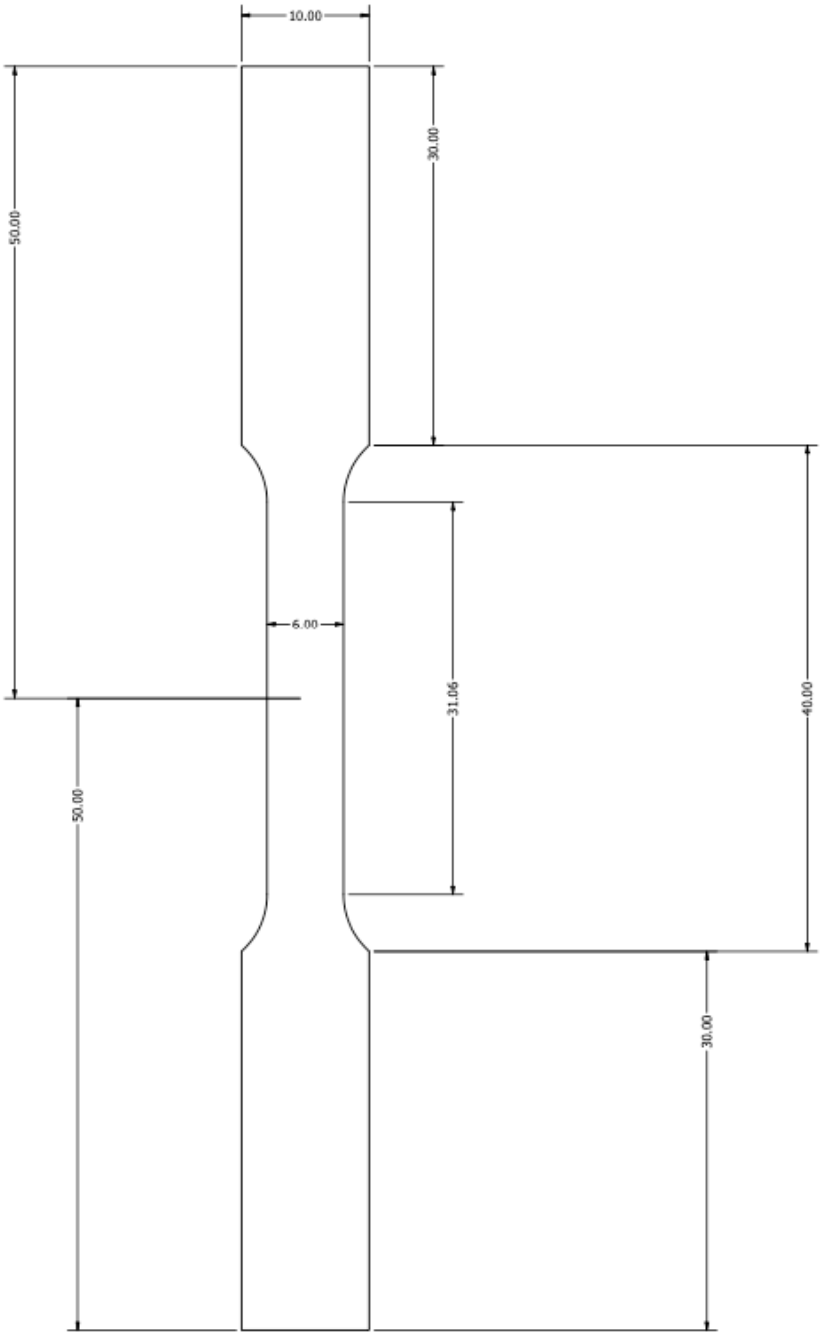

A.2 Cylindrical tensile coupon geometry (units: inches)

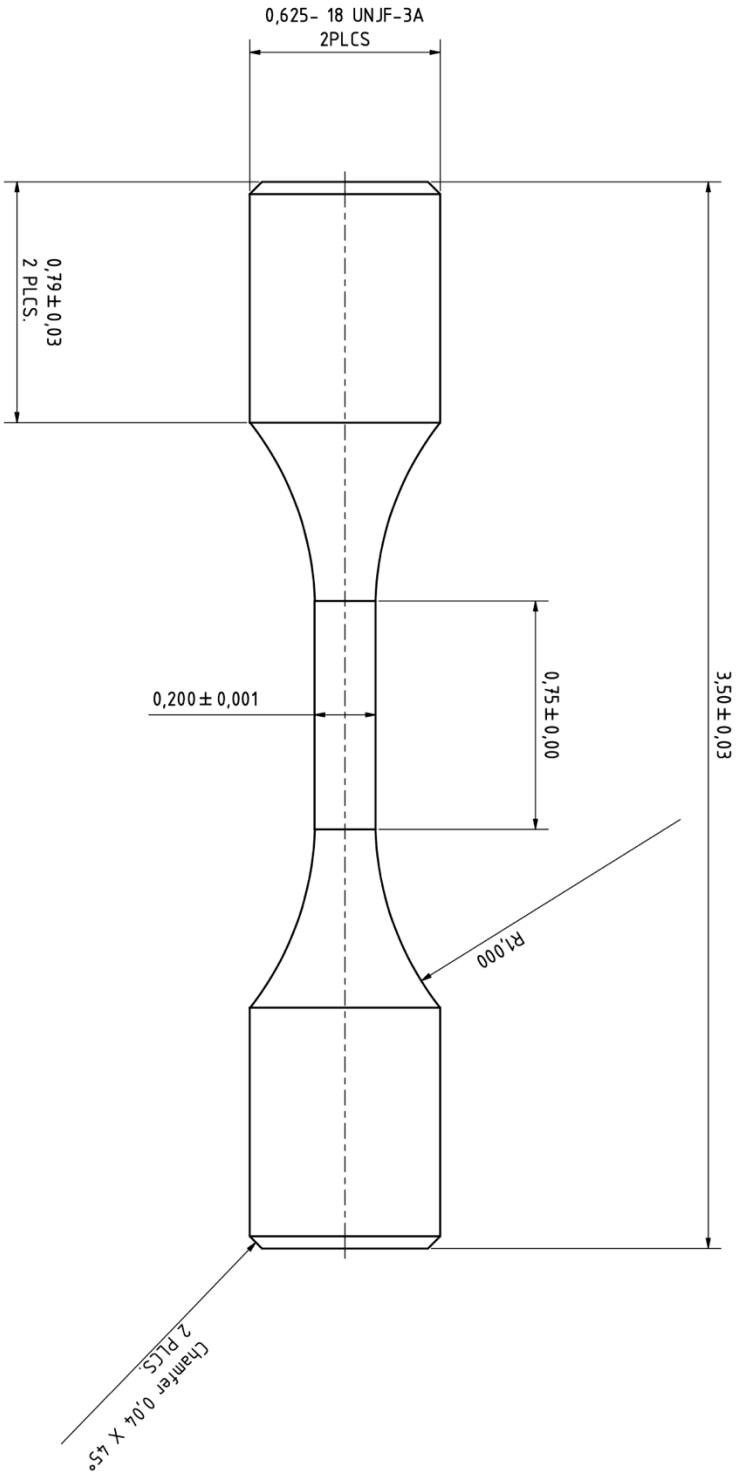

A.3 Micro-tensile geometry for in-situ tensile testing via SEM (units: mm)

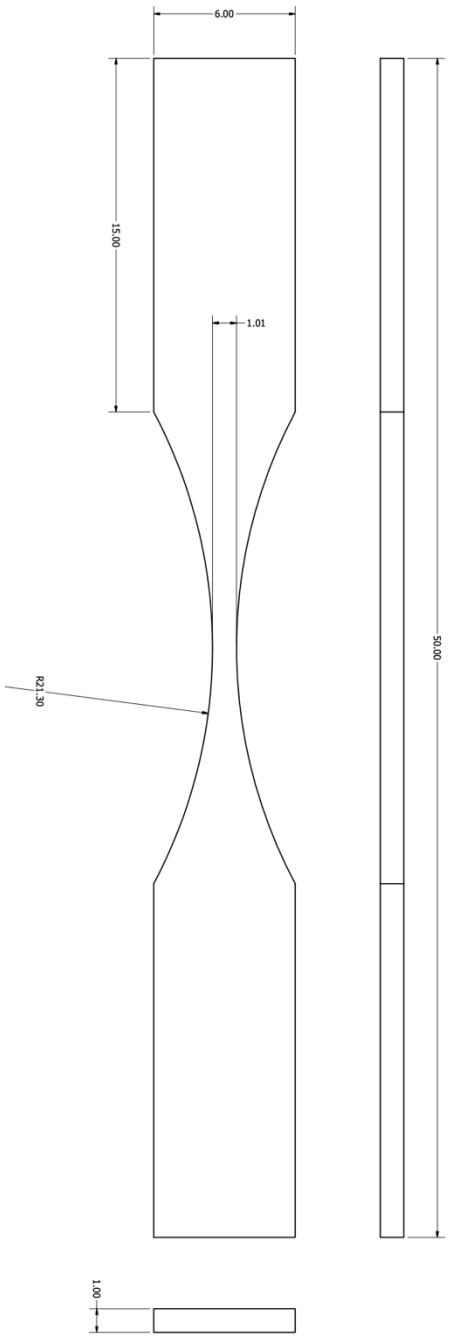

A.4 Micro-tensile test jig with a brief explaination

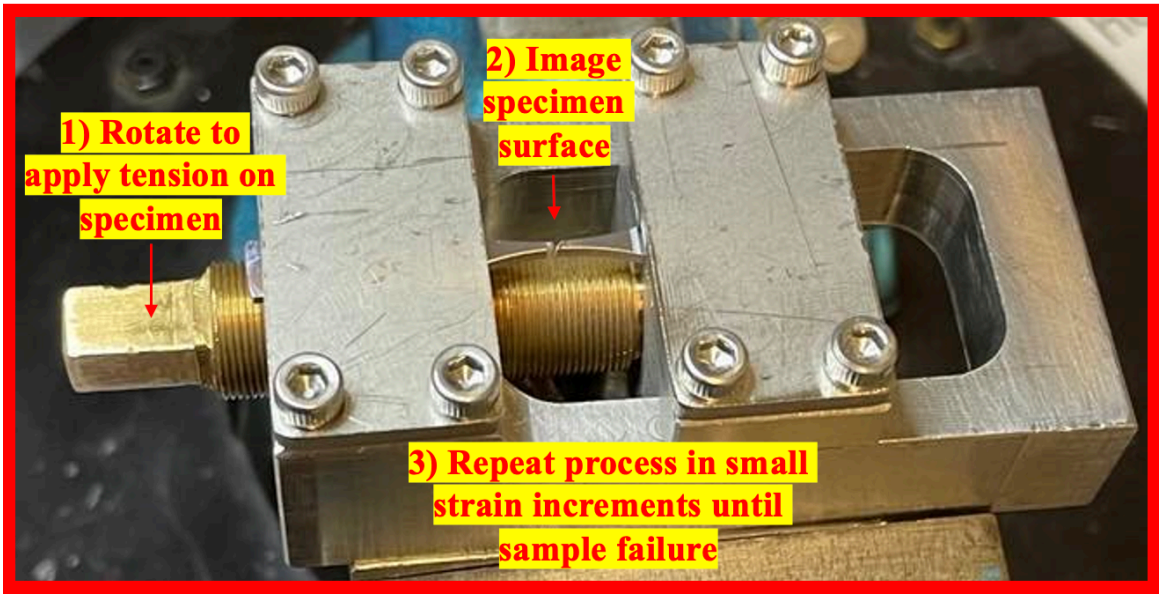

A.5 Tensile coupon for XCT tensile jig (units: mm)